Investigation of mixing characteristics and flow physics induced by spanwise tandem injection in supersonic crossflow

Spandan Maikap and Arun Kumar R.*
Department of Mechanical Enginnering, Indian Institute of Technology Jodhpur, Rajasthan 342030, India

(Received 1 April 2024; accepted 10 September 2024; published 26 September 2024)

This study explores the flow physics and mixing characteristics produced by the interaction of two transversally injected jets along the spanwise direction with a supersonic crossflow using experimental and numerical techniques. Results show that smaller interjet spacing reduces the crossflow entrainment from the top into the interjet region, while wider spacing facilitates greater entrainment. The investigation further reveals that the gap created by the two injected jets allows the crossflow to decelerate and then accelerate to a higher supersonic Mach number as it flows along the interjet region. Investigation of the shock structures revealed that in the case of smaller interjet spacing, the strong part of the two bow shocks created by the transverse jets interacts with each other, whereas with large interjet spacing, the weak part of the two bow shock waves interacts. This leads to a larger local pressure jump in the interjet spacing with a smaller injector gap than the larger one. Various streamwise vortices, such as horseshoe and counter-rotating vortex pairs (CVPs), are seen to form for spanwise tandem injection in crossflow. The interaction of such vortices is seen to be significant in the case with smaller injector spacing compared to the larger one. The oil flow visualization reveals the formation of a herringbone-shaped separation region in the wake of the jets, and the size of this separation zone diminishes with the reduction in injector spacing. The mixing characteristics investigated using Mie scattering and computations reveal that with an increase in injector spacing, the mixing efficiency increases.

DOI: 10.1103/PhysRevFluids.9.093401

I. INTRODUCTION

In the past few decades, hypersonic air-breathing engines incorporating supersonic combustion ramjet engines (SCRAM jet) have been rigorously investigated. However, only limited success has been attained with real-case flight conditions. One of the major difficulties in the realization of SCRAMJET engines is to enable a proper mixing between the supersonic air stream and the injected fuel and to sustain the combustion at supersonic speeds. The residual time available for the fuel to mix with the supersonic air stream is typically in the order of a few milliseconds (ms) due to the high Mach number of the air stream entering into the combustor (typically around Mach 2–4).

One of the most straightforward and dependable techniques to inject fuel in the combustion chamber of a scramjet engine is through a circular orifice in the transverse direction [1–3]. The transverse jet injection has the advantage of high penetration, better mixing, acceptable pressure loss, and no external cooling required. The intricate flow structures and shock waves produced by the transverse injection into crossflow prompted much research in this area, and the overall flow characteristics have been well reported [2,4,5]; a schematic of this is shown in Fig. 1. One of the

*Contact author: arunkr@iitj.ac.in

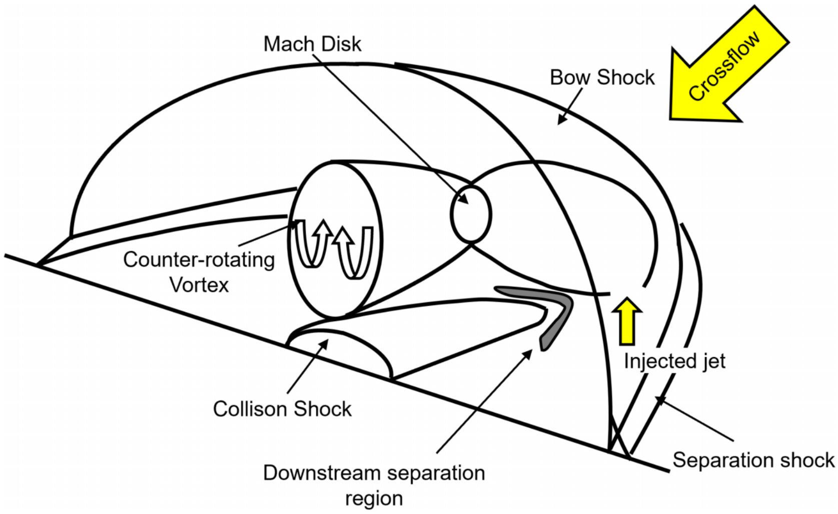

FIG. 1. A schematic of a transverse jet injected into a supersonic crossflow.

most dominant vortex structures in such flows is the counter-rotating vortex pair (CVP), which forms on the lateral side and in the near field of the jet and dominates the far side of the lateral region. The CVP is formed due to the difference in the direction and magnitude of velocities between the injected jet and the crossflow. As the injected jet is normal to the direction of the supersonic crossflow, a skewed mixing layer is formed between the two streams of fluids, resulting in the formation of a hovering vortex and periodically shed vortices in the mixing layer region as reported by Ben-Yakar, Mungal, and Hanson [6]. Moreover, The blockage of the supersonic crossflow by the injected jet also leads to the formation of a bow shock wave upstream to the injection location. The bow shock wave formed upstream to the injected jet creates an adverse pressure gradient near to the boundary layer region. This causes the boundary layers to be separate. The deflection of the crossflow caused by the swelling up of the boundary layer results in the formation of compression waves on top of the separated region. These compression waves merge and form the separation shock waves, which further go on to interact with the bow shock wave and form the λ shock pattern. The vortex region produced by the separated flow is swept in the downstream direction by the crossflow, which results in the formation of a horseshoe vortex pattern around the injection location. The injected jet emanates from the walls and expands into the supersonic crossflow, which produces a flow separation downstream to the injected jet. This separated flow reattaches at a downstream distance and produces a reattachment shock. The injected jet expands, forming expansion fans that further interact with the jet boundary, forming barrel shocks and a Mach reflection shock structure:

$$J = \frac{\rho_j V_j^2}{\rho_\infty V_\infty^2} = \frac{\gamma_j p_j M_j^2}{\gamma_\infty p_\infty M_\infty^2}. \tag{1}$$

The primary advantage of transverse jet injection is its enhanced jet penetration and mixing capability. Although several factors can influence jet penetration, it has been found that these variables can be summarized by a single parameter known as the momentum flux ratio (J) [6–8]. Here ρ, V, M, and p are the density, velocity, Mach number, and static pressure, respectively. The subscript j and ∞ correspond to the jet and the crossflow, respectively. Momentum flux is defined as the ratio of the momentum flux of the injected jet to that of the supersonic crossflow, as given in Eq. (1). Research [7] has shown that increasing the Mach number of the injected jet while maintaining a constant J value leads to a slight increase in penetration. Additionally, studies investigating the injection of different substances, such as hydrogen molecules and ethylene, into a crossflow have revealed that the molecular mass of the fluid significantly affects penetration [6]. To enhance the penetration of the injected jet, it is necessary to increase the momentum flux ratio. However, achieving a higher momentum flux ratio typically requires an increase in the jet's mass flow rate. This presents several challenges for scramjet operation. A significant issue is the stagnation pressure loss caused by the bow shock wave that forms upstream of the injection point. As the jet's momentum increases, the strength of the bow shock also intensifies, leading to greater pressure loss within the combustion chamber. Moreover, a higher mass flow rate can contribute to thermal choking, potentially causing the scramjet engines to unstart.

In recent years, much research has been carried out on using passive flow control devices (which do not require external sources of energy) to enhance the mixing efficiency and thereby augment the combustion efficiency in SCRAMJET combustors. These methods include strut-based injection [9], ramp-based injection [10], pylon-assisted injection [11–15], cavity flame holders [16–19], cantilevered ramp injector [20], and various other combinations. Cavity-based flame holders [16–19] are one of the extensively studied flow control techniques and have the advantage of holding the flame in the recirculating flow created in the cavity. Another proposed strategy for mixing enhancement was to use transverse injection coupled with vortex generators or ramps. The study by Zhang, Liu, and Sun [21] reported that vortex generators placed upstream of the transverse injection jet improved the jet penetration and mixing efficiency. The mixing enhancement is produced by the additional vortices created by the vortex generator. Their study also reported that there exists an optimum distance between the vortex generator and the injected jet where a maximum mixing efficiency can be obtained. The study by Aguilera and Yu [22] reported that the placing of the vortex generator upstream of the injector not only increased the jet mixing characteristics but also reduced the stagnation pressure loss. The study by Vishwakarma and Vaidyanathan [15] proposed that the penetration and spread area of the injected jet increases with an increase in vortex generator height. However, Quan Li, Huang, and Yan [23] observed that regardless of the vortex generator's height, an increase in the jet-to-crossflow pressure ratio resulted in a decrease in mixing efficiency. While passive flow control devices have the advantage of not requiring an external source of energy, they introduce their challenges. Intrusive methods like swept ramps, cavity flame holders, and pylon-based injection generate shock structures within the combustion chamber which induce additional drag, require external cooling, and incur greater pressure loss, resulting in difficulties in the design of the combustion chamber. Furthermore, passive flow control strategies exhibit a limited operational frequency regime, constraining the applicability of such controllers.

Active flow control techniques offer a broad operational frequency range, rendering them a suitable candidate for flow control within a scramjet combustor. Several research strategies involving active flow control methods have been investigated in the past . One such strategy is to inject the transverse jet in a pulsating manner [24–26]. It was reported that the pulsation frequency, amplitude, and waveform shape play a major role in jet penetration [26]. Another method to improve the mixing of the fuel is by using fluidic oscillators [27–30] in supersonic crossflow. Ostermann *et al.* [31] oscillated a fluidic jet in a subsonic crossflow in order to increase the mixing of the two streams. They found that the transient nature of the CVP aided in the mixing process. Maikap and Rajagopal [32] implemented a fluidic oscillator by controlling a transverse sonic jet using two control jets from the sides. They found that the spanwise spread and mixing of the jet were significantly improved when compared to a simple transverse jet.

Although active flow control methods provide a broad range of operational regimes, their reliance on an external energy source necessitates the inclusion of supplementary devices, potentially adding extra equipment and weight to the engine. Another way of the flow control strategy is to inject fuel through tandemly placed injectors in the streamwise direction (one jet behind the other) to increase the overall jet penetration and mixing characteristics [33–35]. This is attributed to the initial jet, positioned against the crossflow, shielding the downstream jets from the high momentum of the supersonic crossflow and thereby facilitating higher penetration of the downstream jets. Lee [35] observed a higher burning rate and increased flame height in tandem injector jets when compared with a single injector. Hollo, McDaniel, and Hartfield [36] explored the impact of interjet spacing between tandem injectors using laser-induced iodized fluorescence. They identified a critical range of interjet spacing where the mechanism governing the mixing rate transitions from vortex-driven to turbulence diffusion. In addition to placing tandem injection in the streamwise direction, which improves the overall jet penetration, multiple jets can be placed in the spanwise direction in tandem with each other. This could increase the overall spread of the jets and thereby increase mixing efficiency. Ali and Alvi [37] reported that in the case of spanwise-tandem injection, for larger injector spacing, the flow is 3D in nature, and for smaller injector spacing, the flow is predominantly 2D in nature. Sebastian and Schreyer [38] extensively investigated the effect of injector spacing in inclined spanwise tandem injection, using Schlieren, oil flow, and numerical techniques. They found that the injector spacing influences the interaction between the multiple vortices in the flow field, which alters the momentum transfer of the fluid. Ali and Alvi [37] also investigated similar flow fields of inclined spanwise tandem injection in which they found that the injector spacing plays an important part in momentum redistribution across the boundary layer, and therefore, such spanwise tandem injections are suitable for boundary layer separation control techniques. Therefore, it is observed that streamwise tandem injection can significantly increase the penetration of the injected jet, albeit with a slight reduction in jet spread. In contrast, spanwise tandem injection enhances mixing by spreading the injected fuel in the spanwise direction, incurring a minor loss in penetration. Nonetheless, both methods ultimately lead to an increase in the mixing efficiency of the injected jet with the supersonic crossflow.

It is thus found from the literature that the tandem injection emerges as a promising strategy with numerous advantages capable of enhancing the mixing characteristics in the scramjet engine. Specifically, implementing spanwise tandem injection can amplify jet spread and, in turn, augment the mixing of fuel with the supersonic crossflow. However, studies on spanwise-tandem injection into a supersonic crossflow are mostly based on the jet structure evolution and boundary layer flow control. The crossflow interaction and mixing characteristics of such injection configurations have not been investigated extensively. In the present study, the interaction of spanwise tandem injection with the supersonic crossflow and the alterations in flow characteristics due to varying injector spacing are systematically examined. Subsequently, these cases are compared with a baseline case featuring a single circular injector, enabling a comprehensive analysis of the resultant enhancement in mixing characteristics.

II. EXPERIMENTAL METHODOLOGY

A. Wind tunnel setup

The experiments were conducted in the supersonic wind tunnel facility established at IIT Jodhpur, India (shock waves and high-speed flow laboratory), as shown in Fig. 2. The experimental facility consists of a $6\,\mathrm{m}^3$ storage tank, which can be charged up to a pressure of 30 bar. High-pressure air is supplied from the storage tank to the settling chamber of the wind tunnel through a 4-inch high-pressure pipeline. A gate valve, a strainer, and an unloading-type pressure regulator valve (PRV) are positioned in the pipeline between the storage tank and the settling chamber. The required settling chamber pressure for tunnel starting is regulated using the PRV. The total pressure in the settling chamber (P_{01}) is measured using a piezo-resistive sensor of Keller make (Keller PA-21Y, accuracy $\leqslant 0.5\% FS$). The wind tunnel was operated with a settling chamber total pressure of $P_{01} = 3\,\mathrm{bar}$ and stagnation temperature T_{01} of 303 K. The exit of the settling chamber was connected to a convergent-divergent (CD) nozzle with an area ratio $A/A^* = 2$, corresponding to an isentropic Mach number of 2.2. The supersonic nozzle profile is designed using the method of characteristics. The test section Mach number is experimentally measured using the stagnation pressure (measured with a pitot probe) and static pressure values obtained in the test section during the blowdown operation, with a settling chamber pressure $P_{01} = 3\,\mathrm{bar}$. Figure 3(a) shows the Schlieren image showing the pitot probe inserted into the test section while the supersonic crossflow is established in the test section. The placement of the pitot probe inside the test section during the tunnel operation creates a bow shock upstream of the pitot probe. The pitot probe, therefore,

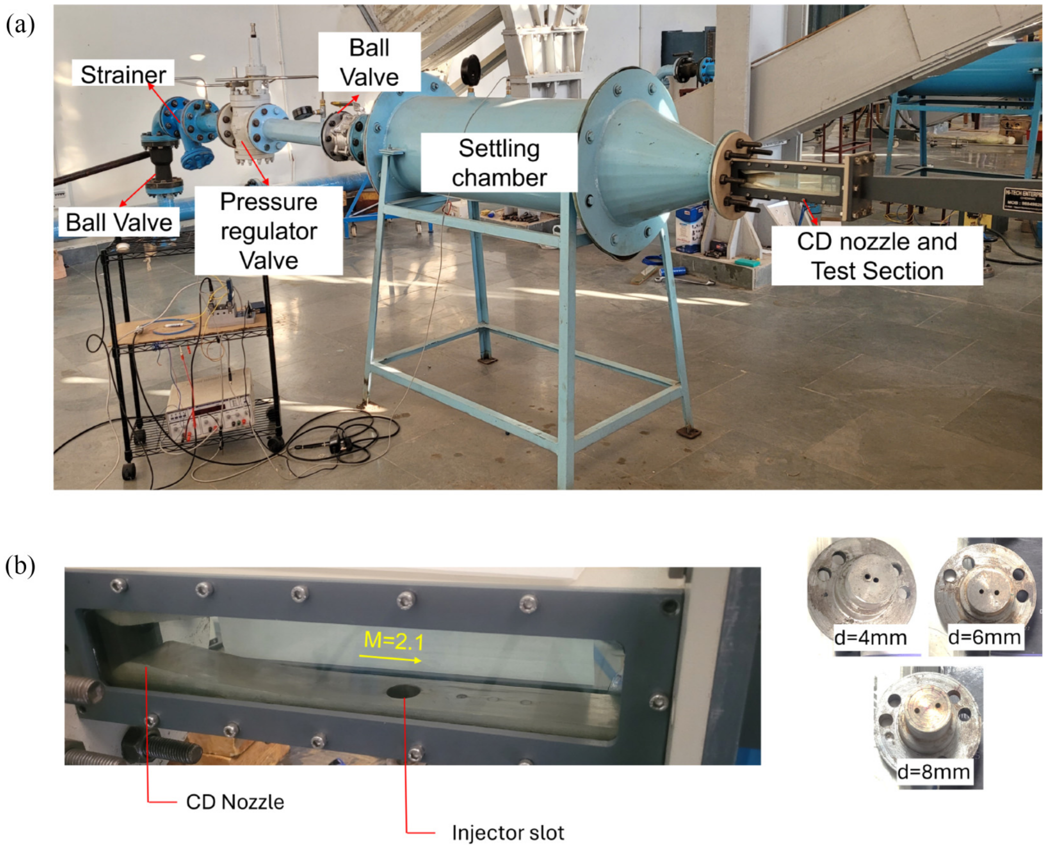

FIG. 2. (a) Supersonic wind tunnel used for studying spanwise-tandem injection in a supersonic crossflow. (b) Actual experimental setup used for studying spanwise-tandem injection (along with the injectors) in a supersonic crossflow.

measures the total pressure (P_{02}) downstream to the normal shock formed by the blunt end of the probe. The static pressure upstream of the bow shock wave is measured through a static pressure port provided in the side wall. The location of the static pressure port and the pitot probe can be identified from the Schlieren image as two dark contrast regions, with the first representing the shadow of the pressure tube from the static port and the second showing the pitot stem's shadow. The static pressure (P_1) measured in the test section is 0.284 bar. The tunnel Mach number can be found from the ratio P_1/P_{02} utilizing the normal shock theory [39]. The experiments are repeated several times to find the repeatability, and the standard deviation of these measurements gives the error in the experimentally measured tunnel Mach number. It is thus found from the experiments that the CD nozzle supplies a uniform flow of Mach number of 2.1 ± 0.04 to a rectangular test area with a cross section of $40 \times 50\,\mathrm{mm}^2$. The experimentally measured values are found to be slightly lower than the design Mach number. This is due to the boundary layer development in the wind tunnel which is not accounted for in the MoC-based nozzle design. A divergent section is provided at the end of the test section for pressure recovery. The details of the wind tunnel and test section are shown in Figs. 2(a) and 2(b), respectively. The previous study by Maikap and Rajagopal [32] gives a detailed discussion on the wind tunnel calibration.

The bottom surface of the test area is provided with a circular slot that can hold a circular insert, as shown in Fig. 2(b). Two 2 mm holes are provided in the circular insert, placed in tandem in the cross-stream direction (z direction). The injector ducts are drilled throughout the circular insert as

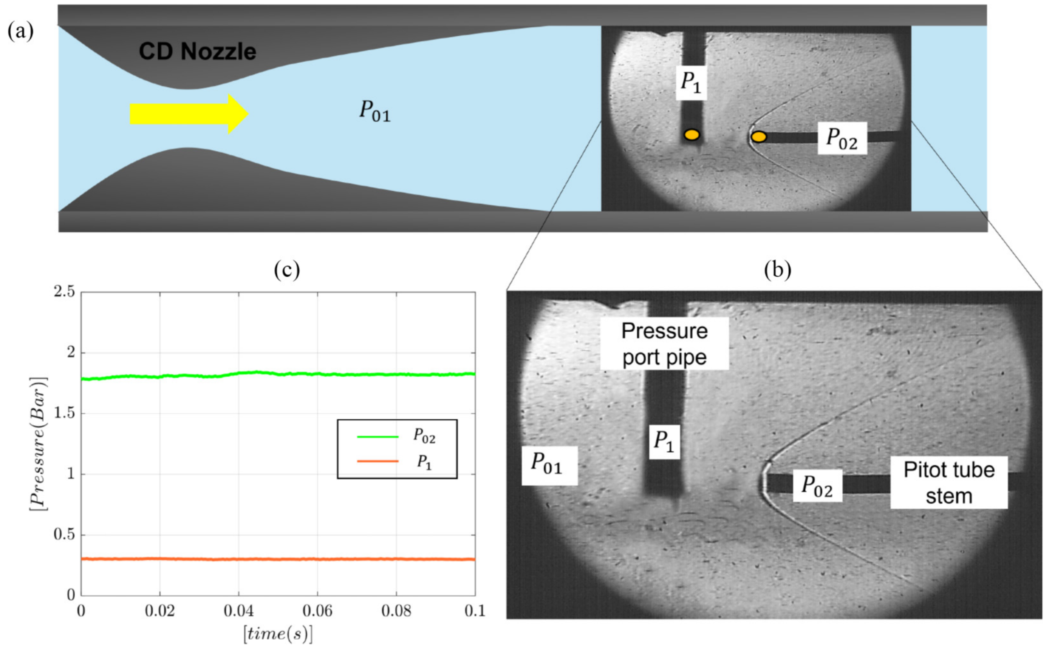

FIG. 3. Wind tunnel calibration: (a) Schematic of the CD nozzle and the test section with pressure port and pitot tube. (b) Enlarged view of the Schlieren images taken under tunnel operation conditions with the pitot probe. (c) Measured static and total pressure obtained from the static pressure port and the pitot probe, respectively.

straight circular ducts. Various circular inserts with different interjet spacing (d) between the tandem injection ports were used to investigate the effect of the injection port gap on mixing efficiency, as shown in Fig. 2(c). A secondary feed line is taken from the storage tank to supply the high-pressure air stream to the injection port. The total pressure of the injected jet ($P_{0j} = 3$ bar) is controlled using a separate pressure regulating valve. A schematic showing the injection system of the spanwise tandem injection jets is shown in Fig. 4. The total pressure of the air stream supplied through the

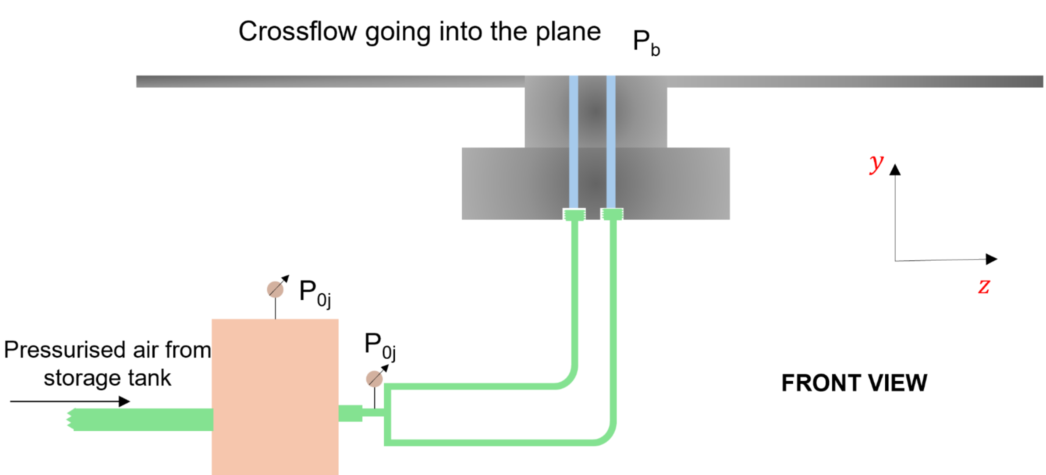

FIG. 4. Schematic of the injection system used in the present study.

TABLE I. Numerical and experimental operating conditions.

Parameters	Values
M_1 (Mach number of the crossflow)	2.1 ± 0.04
P_1/P_{01} (Pressure ration of the crossflow)	0.127
M_j (Mach number of the injected jet)	1
P_{0j} (Total pressure of the injected jet)	3 bar
Pj/P_{0j} (Pressure ratio of the injected jet)	0.5283[a]
J (Momentum flux ratio of the jet)[b]	0.947
Re_∞ (Reynolds number of the crossflow)	100 738[c]
Re_j (Reynolds number of the jet)	88 963
Injectant	Air[d]

[a]Since the injector is a straight circular duct, the flow is choked at the outlet with a pressure ratio of ≈0.5283.
[b]Momentum flux ratio is given as $\frac{\rho_j u_j^2}{\rho_\infty u_\infty^2}$.
[c]The Reynolds number is calculated using the static conditions from the test section, and the characteristic length is chosen as the hydraulic diameter of the crossflow duct.
[d]The crossflow and the injectant are both air, but treated as different species in order to understand the mixing characteristics of the present flow control method.

injection port is also measured using a pressure sensor (P_{0j}). From the measurements, the nozzle pressure ratio P_b/P_{0j} is found to be 0.094. This value is much less than the critical pressure ratio for the sonic condition, and hence, the injection port will be choked with a Mach number of 1 at the exit plane, issuing an underexpanded jet into the cross flow. Four injection configurations have been investigated in the present study. The baseline case consists of a single circular orifice with a diameter of $d_j = d_h = 2.83$ mm, and three tandem injection configurations having injector diameter $d_j = 2$ with different injector spacings ($d = 4$, 6, and 8 mm) were also investigated. For the spanwise tandem injection cases, the orifice diameter of each individual injector is chosen as 2 mm such that the overall area of the two injection ports is equal to the baseline case with a single injector ($d^2_{\text{single}} = 2\times d^2_{\text{tandem}}$). The details of operational conditions and various experimental cases are shown in Tables I and II.

B. Mie scattering

In the present study, the evolution of the injected jet into the supersonic cross flow has been visualized using the Planar Laser-induced Mie Scattering (PLMS) technique. Here, the secondary jet is seeded with olive oil particles using a Laskin nozzle-based seeder (TSI oil seeder 9307) with a mean droplet size of 1 micron. A continuous laser light source (New Age) of 532 nm wavelength and 0.5 W power rating is used to illuminate the test area. The laser beam is converted into a sheet using cylindrical lens-based sheet optics. A DSLR camera (Canon EOS 1500D) with 30 fps and 24 megapixel resolution captures colored images from the Mie scattering experiments. The location

TABLE II. Various cases of spanwise tandem injections.

Cases	Injector diameter (d_j) (mm)	Injector spacing (d) (mm)	Mass flow rate of the injected jet (kg/s)
C0[a]	2.83	–	0.005
CI	2	4	2×0.0025
CII	2	6	2×0.0025
CIII	2	8	2×0.0025

[a]Base line case with a single circular injector [$d_j = d_h$ (hydraulic diameter)].

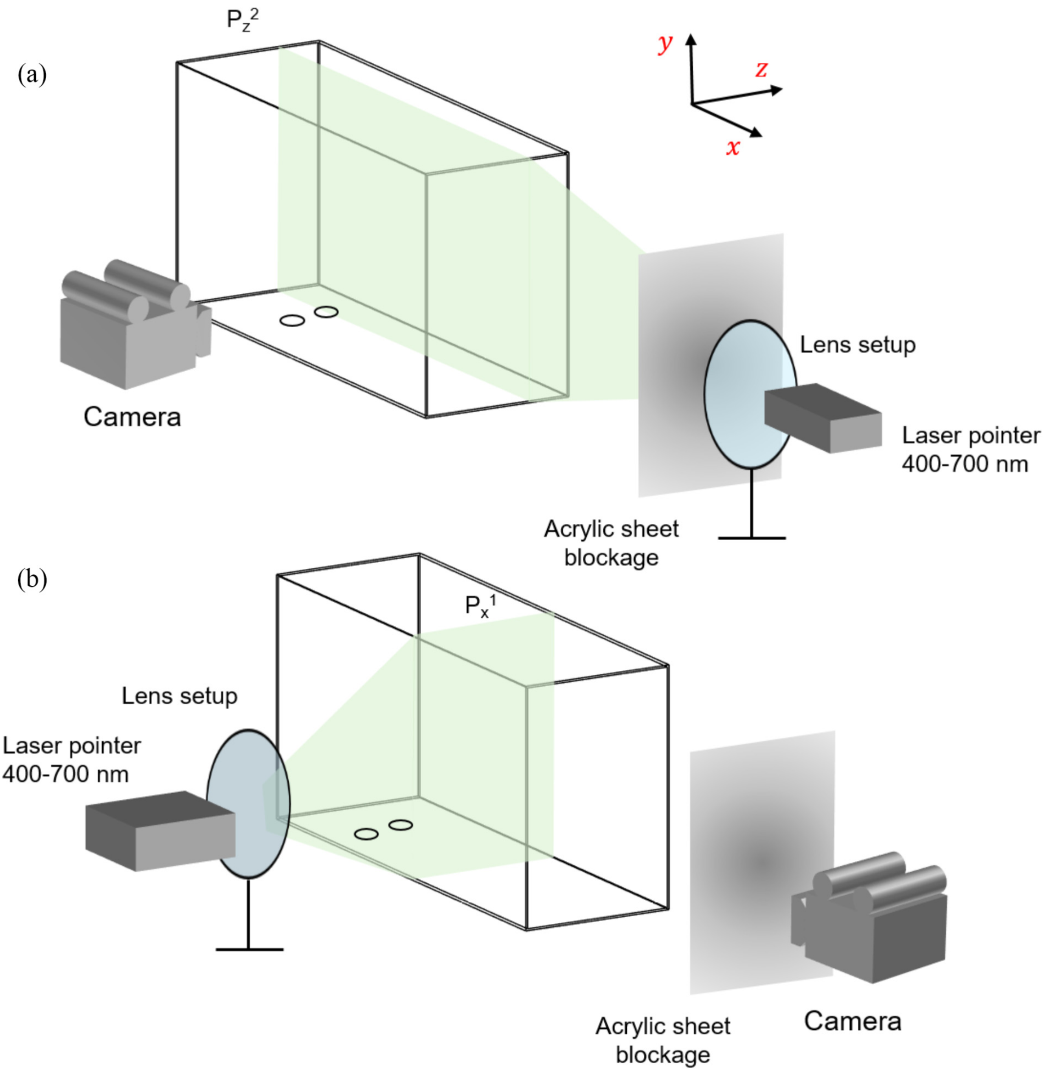

FIG. 5. Schematic representation of the experimental setup used for PLMS imaging. (a) The setup for capturing jet evolution characteristics in a streamwise plane (XY plane) located on the midplane of the left injector (plane: P_z^2) (b) Setup for determining spanwise spread of the injected jet at a spanwise plane (YZ plane) located at $\bar{x} = 6.18$ ($\bar{x} = (x - x_j)/d_h$) (plane: P_x^1).

of the laser sheet is set at two different locations, and Mie scattering images have been captured for two different planes (P_z^2 and P_x^1), as shown in Fig. 5. To capture the streamwise jet evolution characteristics, the laser sheet setup is placed far downstream to the test section covered with an acrylic sheet blockage (to block the airflow impacting the laser setup), as shown in Fig. 5(a). To study the jet characteristics of the individual jets, the laser sheet is placed at a streamwise location plane P_z^2, located at the left injector's midplane. The camera is placed facing the side window. Such a setup is used to find the jet penetration and jet evolution characteristics of the individual jets. To capture the spanwise jet distribution downstream to the injection location, a laser sheet is employed at a cross-stream plane downstream to the injector location by keeping the laser setup towards the side windows and the camera downstream to the wind tunnel, as shown in Fig. 5(b).

TABLE III. Numerical models.

Model type	Details
Working medium	Air
Solver type	Coupled solver
Turbulence model	k-ω SST[a]
Spatial discretization	Second order
Viscosity model	Sutherland
Flux discretization	Roe-FDS (Roe-Flux difference splitting)

[a]A few of the cases are simulated using Improved Delayed Detached Eddy Simulation (IDDES).

C. Schlieren flow visualization

The shock structures produced by the tandem injection were investigated using a z-type Schlieren flow visualization technique. A 100 W quartz-tungsten-halogen light source (Newport) was used to illuminate the test area. The light from the bulb is focused on a rectangular vertical slit using a condensing lens to generate an extended light source. The extended light source is kept at the focus of the first field mirror (a concave mirror with a 200 mm diameter and 1000 mm focal length) to produce a collimated light beam that passes through the side glass of the test section and falls on the second field view mirror. Time-resolved Schlieren images of the test area are imaged using a high-speed camera (Chronos 2.1 HD). The images are recorded at 1000 frames per second (fps), with a light exposure time of 10 μs. The images are obtained at the largest frame size of 1024×576 pixels and at a pixel resolution of 0.1412 mm/pixel.

III. COMPUTATIONAL METHODOLOGY

A. CFD domain

A rigorous CFD campaign has been carried out in the present study to complement the experimental findings. The numerical simulations were carried out by solving the 3D compressible steady Reynolds-averaged Navier-Stokes (RANS) equations using a commercial solver (Ansys-Fluent 2022 R2). Air is considered the working medium, and its state equation is solved using the ideal gas equation. Viscosity changes due to temperature variations are determined using Sutherland's method. Turbulent flow is modeled using the SST k-ω turbulence model, incorporating separate transport equations for turbulence kinetic energy (k) and specific dissipation rate (ω). Previous research suggests that the SST k-ω turbulence model tends to more accurately predict internal flows featuring flow separation compared to other existing models [40,41]. This model's improved performance, consideration of anisotropy, near-wall treatment, robustness, and applicability to complex geometries contribute to its enhanced prediction of separated flows. Given the presence of supersonic flow with flow separation in this study, the SST k-ω turbulence model is considered an ideal choice to characterize turbulence. The governing equations—mass, momentum, and energy—are solved in a coupled manner, with cell center values extrapolated to face centers using a second-order upwind scheme. Roe-Flux difference splitting is utilized to determine convective fluxes across cells, while gradients are computed employing the least squares-based method. In the present study, the supersonic crossflow and the injected jet are considered air. However, separate species transport equations have been solved for the crossflow and the injected jet. A detailed description of the computational flow conditions is given in Table III.

Although the k-ω SST turbulence model effectively captures averaged flow features, it falls short of accurately representing transient phenomena such as shear layer instability, vortex shedding, and shock oscillation. To better simulate the transient dynamics of the injected jet, this study employs an improved turbulence model known as the Improved Delayed Detached Eddy Simulation (IDDES).

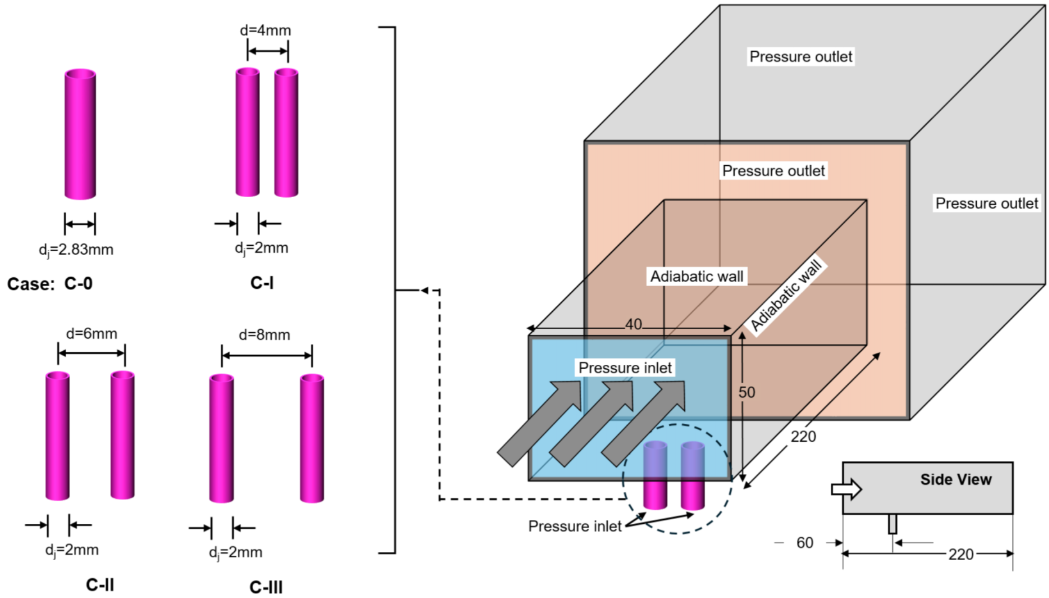

FIG. 6. Schematic representation of the computational domain used for the simulations of various cases of spanwise-tandem injection in a supersonic crossflow.

Delayed Detached Eddy Simulation (DDES) is an excellent choice for resolving flow turbulence in the core flow region. The DDES model employs Large Eddy Simulation (LES) in the core flow, where large-scale turbulent structures are predominant, and uses the k-ω SST model in the near-wall region. This approach effectively captures turbulent structures while minimizing computational costs, providing a balance between accuracy and efficiency in complex flow simulations.

DDES remodels the dissipation of turbulent kinetic energy by multiplying a factor (Y_k) by the dissipation of turbulent kinetic energy equation:

$$Y_k = \rho \beta^* k F_{DDES.} \tag{2}$$

Here ρ, β^*, k are density, low Reynolds correction constant, and turbulence kinetic energy, respectively. F_{DDES} is a conditional variable that is either 1 (for the k-ω model) or a variable depending on the turbulence length scale, the maximum local grid spacing, and a calibration constant. The factor F_{DDES} enables us to switch between the two models.

The computational domain consists of a rectangular crossflow-duct having a cross section of $40\times50\,\text{mm}^2$ with a length of 220 mm, as shown in Fig. 6. The supersonic crossflow with Mach number 2.1 is established in this section by defining the inlet boundary condition (BC) as pressure inlet BC with $P_{01} = 3\,\text{bar}$ and $P_1 = 0.28\,\text{bar}$. The choice of pressure inlet boundary condition is because the total pressure conditions at which the tunnel is operated are known from the experimental measurements and can be used for the computational study. This boundary condition leads to a scenario similar to a developing boundary layer in the bottom wall where the injector is placed. The turbulence quantities at the inlet are specified using the turbulence viscosity ratio and turbulence intensity. The given turbulence intensity is 5%, and the viscosity ratio is 10. The transported quantities of turbulence [turbulent kinetic energy (k) and dissipation rate (ϵ)] are then computed using the input value of turbulence intensity and viscosity ratio by the solver.

A larger rectangular domain follows the crossflow duct. This larger domain is given to mimic the ambient condition prevailing at the exit of the crossflow duct. The outer domain is given a pressure outlet boundary condition with a static pressure of 1.01 bar. The transverse injection into the crossflow is carried out using two circular ports, which are tandemly placed in the spanwise

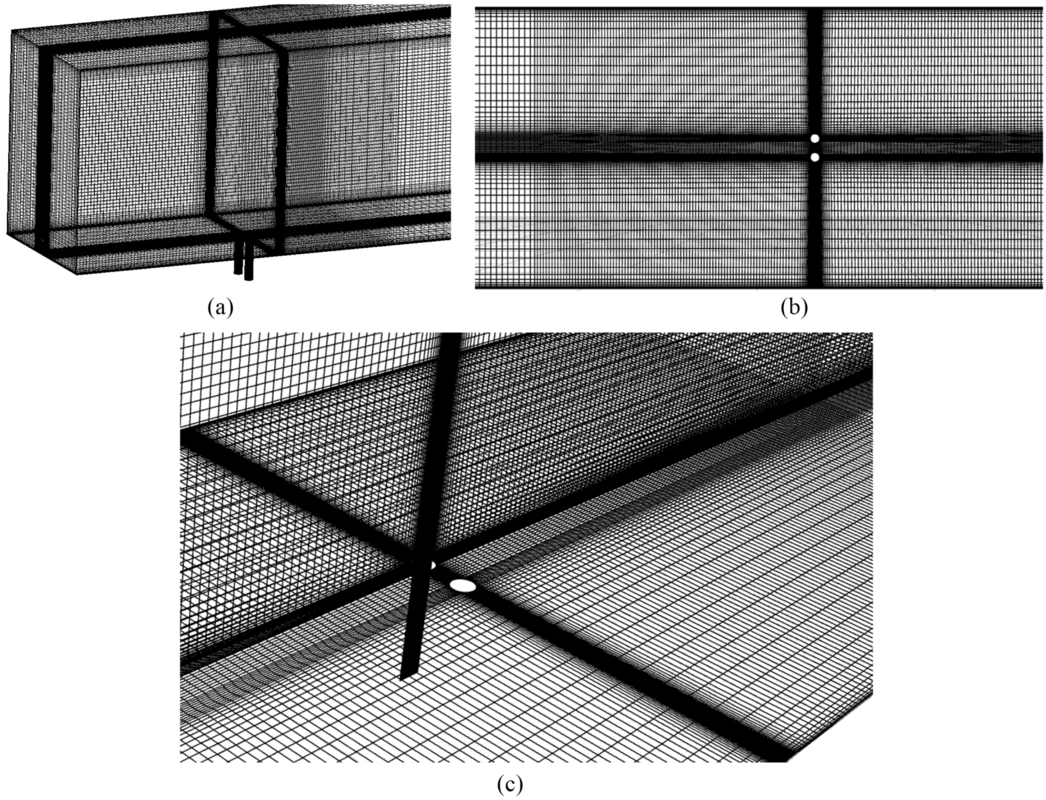

FIG. 7. Grid structure: (a) front isometric view, (b) top view, and (c) top isometric view along with the cut section at the central plane of the mesh used for the spanwise tandem injection simulation.

direction with various cases of injector configurations (Case: C0, CI, CII, and CIII). A baseline case (Case: C-0) with a single circular injection port is also simulated in the present study. The injection port diameter for the baseline case is 2.83 mm, whereas the port diameter for the tandem injection case is 2 mm, such that the total area of the tandem injection ports will be nearly the same as that of the baseline case with a single injection. The details of the various computational cases are given in Table II.

B. Mesh independence and code validation

A 3D hexahedral unstructured mesh is created in the computational domain using ICEM CFD software for various cases (C-0 to C-III), as shown in Fig. 7. To accurately simulate the boundary layer created by the crossflow, the wall boundary is assigned a minimum mesh size, with a transverse height of 0.04 mm for the first layer and a growth rate of 1.2. A comprehensive mesh independence study has been carried out for case C-I, with three distinct mesh sizes comprising 2 million, 3 million, and 4 million cells. The nondimensional bottom-wall static pressure variations at the crossflow duct's centerline [$\bar{y} = 0, \bar{z} = 0$] are compared for these three grid spacings, as shown in Fig. 8(a). Notably, the nondimensional pressure variations for 3 million and 4 million cells closely align with each other, indicating that the dependence on grid spacing diminishes beyond a mesh size of 3 million cells. Consequently, the mesh with 3 million cells is selected for the simulations conducted in this study.

For validating the CFD code, two different modes of validation are utilized in the present work. The first type of validation consists of a static wall pressure measurement for a transverse

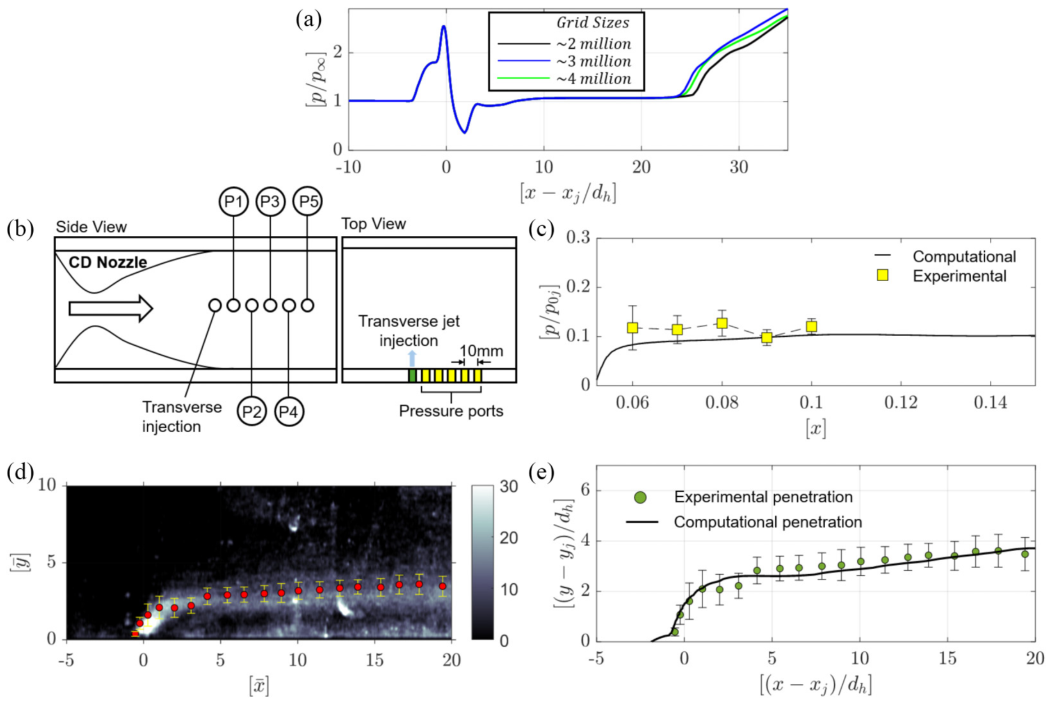

FIG. 8. (a) Nondimensionalized static pressure at the duct bottom wall centerline $[\bar{y} = 0, \bar{z} = 0]$ $[\bar{y} = (y - y_j)/d_h$ and $\bar{z} = z/d_h]$ for various grid sizes. (b) Schematics of the experimental setup used for validation study. (c) Wall static pressure obtained from the validation experiment and comparison of the same with the computationally obtained result. (d) A PLMS image at a plane P_z^2 overlaid with the locus of points having 10% of the maximum light intensity for the single injector case. This image shows the technique used to find the experimental jet penetration for validation. (e) Comparison of numerical and time-averaged experimental jet penetration. The errors are multiplied by 2 for better image clarity.

jet in a supersonic crossflow. In a separate experimental setup [see Fig. 8(b)], a transverse sonic jet is introduced into a supersonic crossflow with a Mach number of 2.1. The computational fluid dynamics (CFD) code utilized in this study is applied to simulate the flow dynamics. The transverse jet is introduced through a 2 mm diameter circular port located at the side walls of the test section [refer to Fig. 8(b)]. Downstream to the injector, five wall static pressure ports (P1, P2, P3, P4, and P5) with circular orifices (diameter = 2 mm) are positioned, each spaced 10 mm apart. The transverse jet is supplied at a pressure of 3 bar, and the supersonic crossflow is maintained at a total pressure of 3 bar and static pressure of 0.28 bar, resulting in a Mach number of 2.1 in the test section. The wall-static pressure is measured using a piezo-resistive pressure sensor of Keller make (M5HB type with accuracy: 60:1 FS, sampling rate of 50 kHz). The pressure sensors are connected to the pressure ports via polyurethane pipes to record the pressure data at a sampling rate of 50 kHz. The transverse jet manifests as an underexpanded jet due to the provided pressure ratio. Computational simulations are conducted with conditions mirroring the experimental setup. The average wall static pressure values at different monitoring locations, obtained through experimental measurements and computational predictions, are presented in Fig. 8(c). The computed wall static pressures closely match the experimentally measured values. The minor discrepancies can be attributed to the relatively larger size of the measuring port and inherent inaccuracies associated with turbulence modeling in simulations. Consequently, the validation study demonstrates the adequacy of the present CFD code in predicting the flow field for scenarios involving the injection of a transverse jet into a supersonic crossflow.

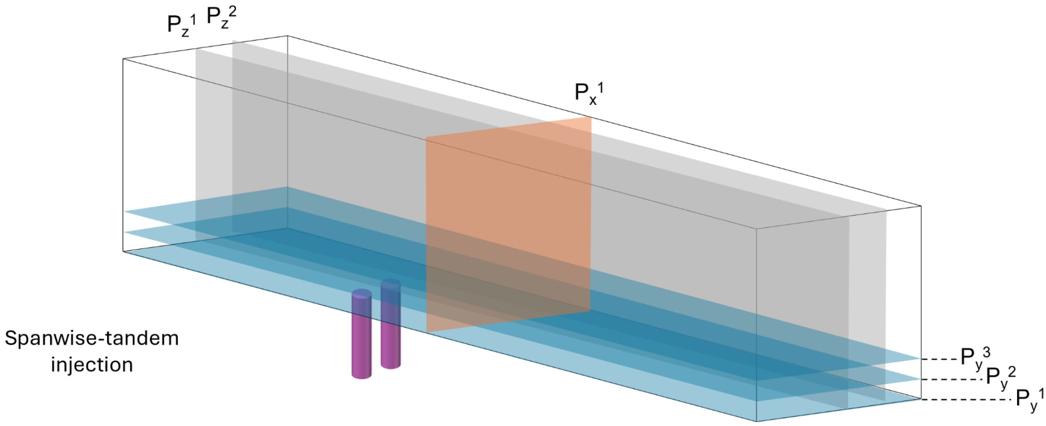

FIG. 9. Schematic representation of the various planes considered for investigating the flow features involved in the present study.

The second type of code validation consists of comparing the injected jet penetration into the crossflow obtained from the computations and the experiments for case C-0 (baseline case with a single circular injector). The penetration from computations is calculated by finding the transverse location at which the mass fraction value of the injected jet is 0.1 at a duct center plane [$\bar{z} = 0$]. The experimental penetration is calculated with the help of PLMS images. Multiple PLMS images are taken with the same operating conditions, and a time-averaged PLMS image is used to find the jet penetration. The error is calculated by taking the standard deviation of the penetration values from the mean value. The details of the method of finding the penetration through PLMS are given in Sec. IV B 1. The penetration obtained from the numerical and experimental methods matches closely, further establishing that the current CFD code is sufficient to accurately predict the flow patterns in situations where a transverse jet is introduced into a supersonic crossflow.

IV. RESULTS AND DISCUSSIONS

In this section, two major aspects have been discussed: (1) the general flow features produced by the interaction of the spanwise-tandem injection into supersonic cross flow and (2) the overall mixing characteristics of the spanwise tandem injection configuration. A comprehensive investigation of flow characteristics has been carried out at various planes in the flow field, as depicted in Fig. 9. The streamwise planes P_z^1 and P_z^2 are located at the locations [$\bar{z} = 0$] and [$\bar{z} = 0.5d/d_h$] respectively. Here d is the injector spacing (4, 6, or 8 mm). The spanwise plane P_x^1 is located at an axial distance [$\bar{x} = 6.18$]. The transverse planes P_y^1, P_y^2, and P_y^3 are located at transverse locations [$\bar{y} = 0.353$], [$\bar{y} = 0.706$], and [$\bar{y} = 1.06$] respectively.

A. General flow features

1. *Crossflow interaction with the injected jet*

Figures 10(a)–10(d) shows the isosurface of mass fraction ($Y_j = 0.2$) of the injected jet for various injector spacings (cases: C-0 to C-III) from the CFD simulations. The isosurface of mass fraction shows the overall injected jet evolution into the crossflow. It is seen that when the transverse jet is injected into the crossflow, the jet undergoes downstream bending owing to the high momentum of the supersonic crossflow. It can also be seen that the interaction of the injected jet with each other strongly depends on the injector spacing (C-0 to C-III), and this, in turn, is expected to influence the cross-flow characteristics. With sufficiently large interjet spacing $d = 6$ and 8 mm, the injected jet emerges as distinct twin jets in the cross-stream flow, whereas, with the decrease in

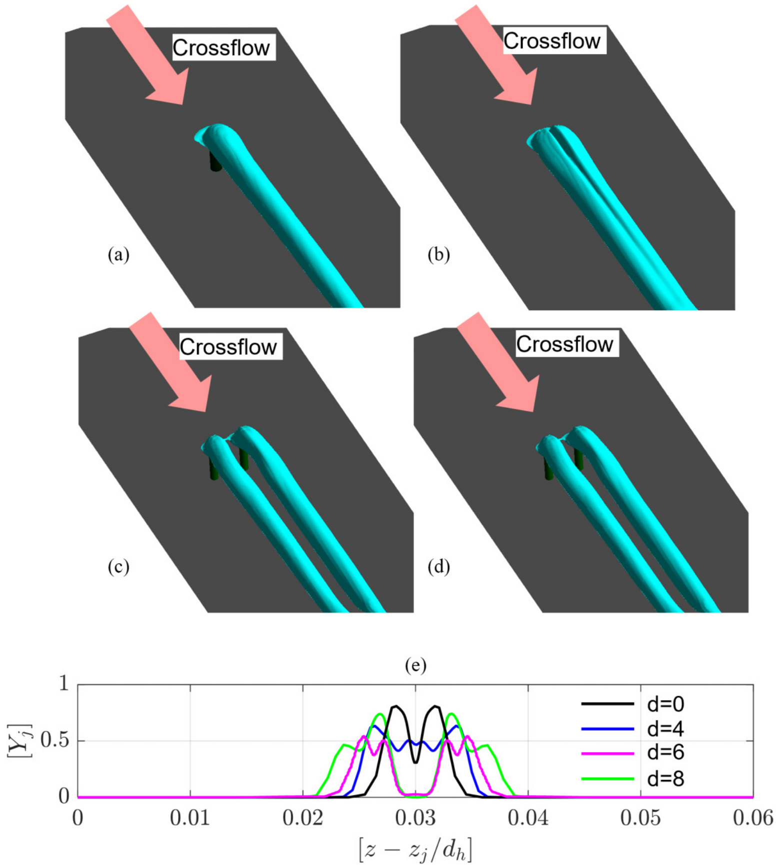

FIG. 10. Isosurfaces of mass fraction ($Y_j = 0.2$) plotted for various cases of spanwise-tandem injection. (a) For the single injector (case: C-0), (b) for $d = 4$ mm (case: C-I), (c) $d = 6$ mm (case: C-II), and (d) $d = 8$ mm (case: C-III). (e) Plot showing the mass fraction distribution at a line spanning in the z direction, downstream to the injectors [$\bar{x} = 2.65$, $\bar{y} = 0.353$] for various cases (C-0 to C-III).

interjet spacing, the two jets start to interact with each other (case C-I). The interaction of jets with closely spaced injectors can also be seen from the mass fraction distribution along the spanwise direction (z direction) at [$\bar{x} = 2.65$, $\bar{y} = 0.353$], as shown in Fig. 10(e). For lower injector spacing ($d = 4$ mm), the injected jet mass fraction value in the intermediate space between the two jets shows a higher positive value ($\bar{Y}_j > 0.50$), which clearly indicates the interaction of the injected jet between each other. For the case of higher injector spacing ($d = 6$, 8 mm), the mass fraction value in the intermediate space between the two jets is zero, which confirms the noninteraction of the two jets.

Figure 11 shows the mass fraction contours overlaid with the streamlines in the y-z planes (planes: P_x^1, P_x^2, and P_x^3) obtained from CFD simulations, which are at various streamwise locations (x axis) for different injector spacing (cases: C-0 to C-III). In the baseline case with a single injector (C-0) [Figs. 11(a)–11(c)], the injected jet mass fraction is distributed in two kidney-shaped regions. This occurs due to the well-known CVPs that arise when a transverse jet interacts with a supersonic crossflow. Due to the sense of the rotation of CVPs, the injected jet is lifted upwards, thus enabling penetration of the jet into the supersonic crossflow. In contrast to the single jet, in the case of spanwise tandem injection cases (C-I to C-III) [Fig. 11(d)–11(l)], the mass fraction is distributed in the region created by two distinct pairs of CVPs. In the case of $d = 4$ mm (C-I), the two jets are close enough to interact with each other in the central plane, thus causing the two CVPs to interact

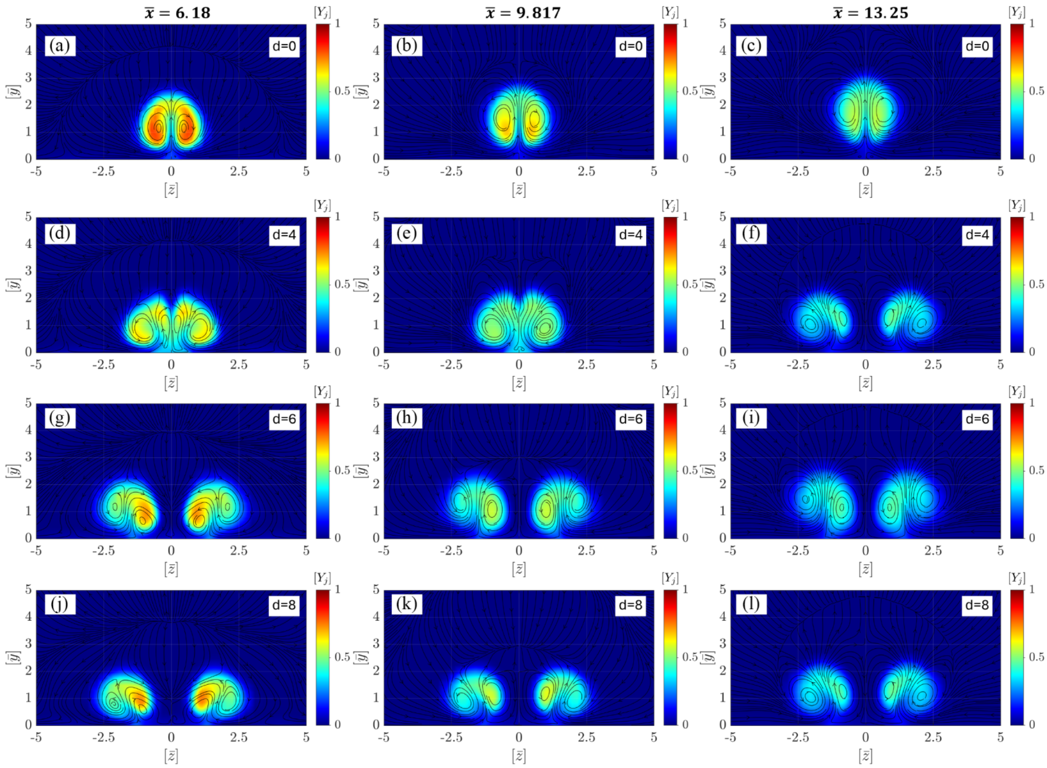

FIG. 11. Mass fraction contours overlaid with the streamlines at spanwise planes (yz plane) located at various downstream axial distances ($\bar{x} = 6.18$, $\bar{x} = 9.817$, and $\bar{x} = 13.25$) for various cases: (a)–(c) single injector, case C-I, (d)–(f) $d = 4$ mm, case C-II, (g)–(i) $d = 6$ mm, case C-II, and (j)–(l) $d = 8$ mm.

with each other. The sense of rotation of the adjacent pair of CVPs hinders the jet penetration and causes a portion of the injected jet to stay near the wall, as shown in Figs. 11(d) and 11(e). As the injector spacing increases to $d = 6$ and 8 mm, the mass fraction is again distributed in the CVP regions [see Figs. 11(g)–11(i) and Figs. 11(j)–11(l)]. As the spacing is large in this case, the CVPs do not interact with each other. This results in the isolation of the two jet regions, and thus, the downward flow of the injected jet is not seen in Figs. 11(g)–11(i).

Additionally, as the CVPs are formed, it entraines the crossflow and enables extensive mixing between the supersonic crossflow and the transverse jet [42]. For the case with the lower injector jet spacing (case C-I), the supersonic crossflow is restricted from entering the interjet region from the top side. This can be seen from Figs. 12(a)–12(c), which shows the y components of the velocity overlaid with the streamlines at a yz plane (P_x^1) for various cases (C-I to C-III). It can be seen from Fig. 12(a) that in the case of $d = 4$ mm (C-I), the negative y-velocity region is contained only in the top region of the CVPs and does not extend to the region between the two jets. This is because the interaction of the injected jet restricts the cross-flow jet from penetrating the interjet space. As the injector spacing is increased to $d = 6$ and 8 mm [Figs. 12(b) and 12(c), respectively], the negative y velocity extends into the region between the CVPs. This is due to the supersonic cross-flow filling the gap between the two injected jets from the top side.

These effects can be further seen from the contours of the z-velocity component overlaid with the streamlines at a yz plane (P_x^1) obtained numerically, as shown in Figs. 12(d)–12(f). In the case of $d = 4$ mm [Fig. 12(a)], the overall z-velocity contour depicts distinct zones of positive and negative values across the symmetry line [$\bar{z} = 0$]. On the right side of the symmetry line, a positive z velocity

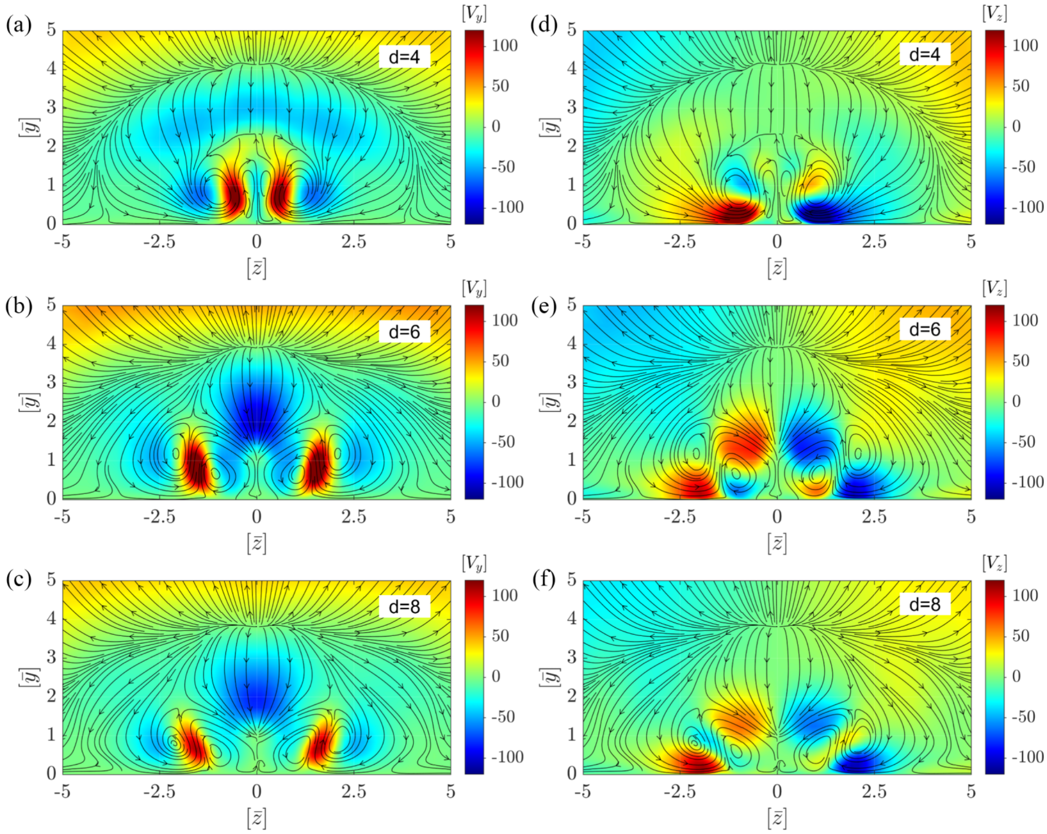

FIG. 12. Contours of (a)–(c) y component of the velocity and (d)–(f) z component of the velocity plotted at a spanwise plane (P_x^1) for various cases (C-I to C-III).

followed by a negative value can be observed, and this shows the rotational flow in the spanwise plane caused by the streamwise vortices (CVPs) formed in the injected jet. A similar z-velocity distribution with opposite contour level values can be seen on the left side of the symmetry plane. This shows the CVPs formed in the injected jet from the left side. A detailed discussion of the various dominant vortex patterns is given in Sec. IV A 4. Additionally, it can be seen from the streamlines that the supersonic crossflow enters the interjet region for the cases with injector spacing $d = 6$ and 8 mm (C-II and C-III). In contrast, for the $d = 4$ mm case, the supersonic crossflow is not able to enter the interjet region due to strong jet-jet interaction. The supersonic crossflow entering from the top side of the two jets compresses the flow field from the top side. It significantly changes the shape of the streamwise vortex structures, which is discussed in Sec. IV A 4.

The flow characteristics in the crossflow surrounding the two tandem-spanwise jets depend on the injector spacing (d). This is investigated numerically by plotting the Mach number contour overlaid with the streamlines at various transverse planes (P_y^1, P_y^2, and P_y^3) located at various transverse locations ([$\bar{y} = 0.353$, 0.706 and 1.06] respectively), as shown in Fig. 13. Figures 13(a)–13(c) show the Mach number contour at various transverse locations for case C-I. The Mach number contours at a plane that is closer to the wall (P_y^1) initially show a region of subsonic flow, which is caused by the separation zone created by the bow shock wave-boundary layer interaction, as shown in Fig. 13(a). The subsonic crossflow enters the region between the two injectors, creating a convergent-divergent passage (bottleneck region) that allows the crossflow to pass through. As a result, the crossflow locally accelerates to a higher supersonic Mach number, as seen in Fig. 13(a). Meanwhile the wake

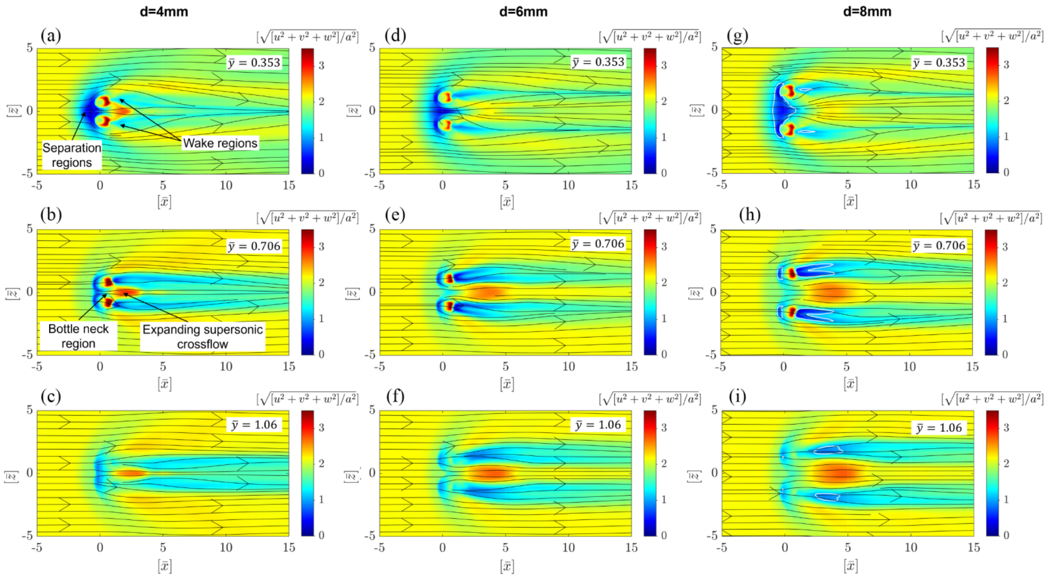

FIG. 13. Mach contours at different transverse planes (P_y^1, P_y^2, and P_y^3) overlaid with the projection of streamlines in the x and z direction for various spanwise tandem injection cases: (a)–(c) C-I, (d)–(f) C-II, and (g)–(i) C-III.

region produced by the injected jet leads to the flow separation downstream to the injector location and produces recirculation bubbles. This results in the formation of a low-velocity crossflow jet region downstream to the injected jet as found in the previous literature [43,44]. Further discussion on the wake region can be in Sec. IV A 3. Thus, a complex subsonic-supersonic crossflow region exists closer to the bottom wall. Similar Mach number profiles are seen for the $d = 6$ and 8 mm cases (C-II and C-III), as shown in Figs. 13(d) and 13(g). At a transverse plane that is slightly above the wall P_y^2, the overall Mach number profile remains nearly the same for the three cases C-I [Fig. 13(b)], C-II [Fig. 13(e)], and C-III [Fig. 13(h)] since the considered plane (P_y^2) is still under the separation region created by the bow shock wave- boundary layer interaction. Additionally, the Mach disk formed by the underexpanded sonic jets is visible in this plane, located downstream of the jets. At a transverse plane above the separation zone (P_y^3), the extensive flow separation region does not manifest in the Mach contours. Nevertheless, the deceleration of the crossflow due to the two bow shock waves produced by the injected jet can be clearly observed. The two bow shock waves meet at the midplane, creating a shock wave reflection. For the case with $d = 4$ mm (C-I), the strong part of the two bow shock waves interacts at the midplane, thus creating a subsonic patch behind the shock front, as shown in Fig. 13(c). With the increase in the injector spacing, the weaker part of the bow shock waves interacts, thus creating a supersonic patch near the midplane behind the shock front. The crossflow accelerates after passing through the passage between the two tandem-spanwise injectors and forms a higher supersonic region, as shown in Figs. 13(c), 13(f), and 13(i). Note that the supersonic flow region downstream of spanwise-tandem injections is more extensive in the case of $d = 8$ mm compared to $d = 6$ mm and, consequently, $d = 4$ mm. This can be attributed to the larger injector spacing, which allows for increased space for crossflow expansion and acceleration. A detailed discussion on the shock wave characteristics is given in Sec. IV A 2.

2. Shock wave characteristics

It is well known that the transverse jet injection into supersonic cross-flow acts like a blockage and forms a bow shock upstream to the injection location. This can be seen from the Schlieren images taken at the plane P_z^2 (for plane reference, see Fig. 9), as shown in Figs. 14(a)–14(d). The bow shock wave upstream to the jet creates an adverse pressure gradient, which causes the incoming boundary layer of the freestream to separate, forming a separation shock, which can also be seen in the Schlieren images. As the sonic jet emanates from the injector, it expands further into an underexpanded jet. The expansion fans produced in the underexpanded jet interact with the jet boundary (which is an open boundary) and thus form compression waves. These compression waves merge and form the barrel shock wave. The barrel shock further terminates as a Mach disk (MD), as shown in the zoomed view of the shadowgraph image in Fig. 14(a). Figures 14(b)–14(d) show the Schlieren images at the center plane of the left injector P_z^2 (for plane reference, see Fig. 9) for the cases C-I to C-III. The overall shock structure remains the same for all the cases of spanwise tandem injection (C-I to C-III) owing to the same flow rate of the injected jet from each injector.

The shock wave interaction characteristics are further investigated computationally with the aid of Mach number and pressure contours at various planes (for plane reference, see Fig. 9). Figure 14(e) shows the contours of Mach number at the streamwise plane P_z^2, which is the midplane of the injector for the baseline case C-0. A bow shock wave (BS) can be seen upstream of the injector. As discussed earlier, this is formed due to the flow obstruction faced by the supersonic crossflow, causing the crossflow stream to bend in the spanwise and transverse direction. Additionally, the bow shock forms an adverse pressure gradient closer to the wall, causing the boundary layer to thicken locally. This results in the formation of the separation shock (SS), as shown in Fig. 14(e). Moreover, the sonic jet can be seen expanding and forming s barrel shock and Mach disk [Fig. 14(e)]. Figures 14(f)–14(h) show the Mach contours at the streamwise plane P_z^2 for various cases of spanwise-tandem injections (C-I to C-III). It can be seen that the transverse height at which the Mach disk is located from the bottom wall has significantly reduced when compared to the baseline case (C-0). This is due to a reduced mass flow rate injected by the individual spanwise-tandem injectors.

For the spanwise-tandem injection cases, two separate bow shock waves, one from each injected jet, are expected to be formed, and the two bow shocks are likely to interact at a spanwise location between the two injectors. This is evident in Figs. 15(a)–15(d), which shows the normalized wall static pressure contours at the bottom wall for various cases. Figure 15(a) shows the wall static pressure at the bottom wall for the baseline case (single injector, $d = 0$). The separation zone and a single bow shock wave are clearly seen in Fig. 15(a). In the case of tandem injection with spacing $d = 4$ mm (C-I), the two bow shocks are seen to interact strongly at the centerline ($\bar{z} = 0$), as shown in Fig. 15(b). A quantitative analysis of the shock interaction can be seen in Fig. 15(e), which shows the wall static pressure variation at the centerline of the duct bottom wall [$\bar{y} = 0, \bar{z} = 0$]. Initially, at [$\bar{x} = -3.39$], the wall static pressure rises smoothly due to the multiple compression waves originating from the separated region. As discussed earlier (see Sec. IV A 2), these compression waves are formed due to the local boundary layer thickening and subsequent separation due to the bow shock wave-boundary layer interaction. Furthermore, it can be seen that the wall static pressure rises rapidly at an axial location [$\bar{x} = -1$] for the case C-I ($d = 4$ mm). This is due to the interaction of the strong part of the two bow shock waves produced by the individual injected jet, which in turn yields a strong compression in the region ($\bar{x} = -1$ to $\bar{x} = 0.2$). Meanwhile, for the case with interjet spacing $d = 6$ and 8 mm (case C-II and C-III), the two bow shocks interact weakly and thereby form weaker compression regions at the duct centerline. This is because, as the interjet spacing increases, the weak part of the bow shock interacts with each other, creating a lower pressure rise, which is reflected in the pressure plot as shown in Fig. 15(e). This phenomenon is illustrated using a schematic in Fig. 15(f). It can also be seen from the wall static pressure plot [Fig. 15(e)] that the separation shock stand-off distance from the injector location is higher in the case of $d = 4$ mm (C-I) as compared to the cases with injector spacing $d = 6$ and 8 mm (C-II and C-III). This is because, for the $d = 4$ mm case (C-I), a larger adverse pressure gradient is created due to the strong interaction of the two bow shock waves. Moreover, two separate V-shaped collision shocks are seen to be formed downstream of the injector location [Fig. 15(a)]. This is formed due to

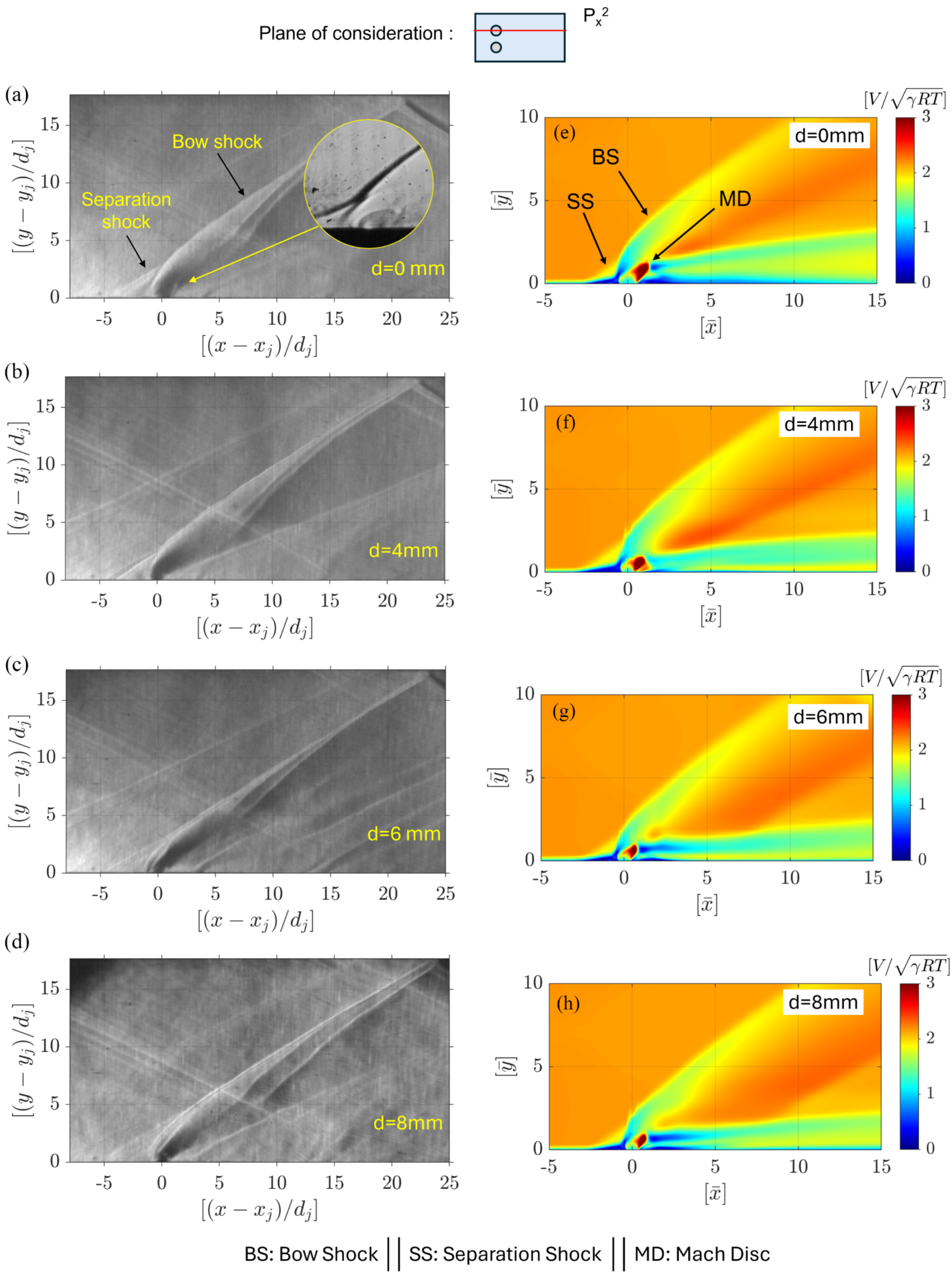

FIG. 14. Schlieren flow visualization images captured at the plane P_z^2 for various cases: (a) C-0 (along with an inset showing shadowgraph), (b) C-I, (c) C-II, and (d) C-III. Contours of Mach number at the streamwise plane located at the centerline of the left injector (P_z^2) for various cases: (e) C-0, (f) C-I, (g) C-II, and (h) C-III.

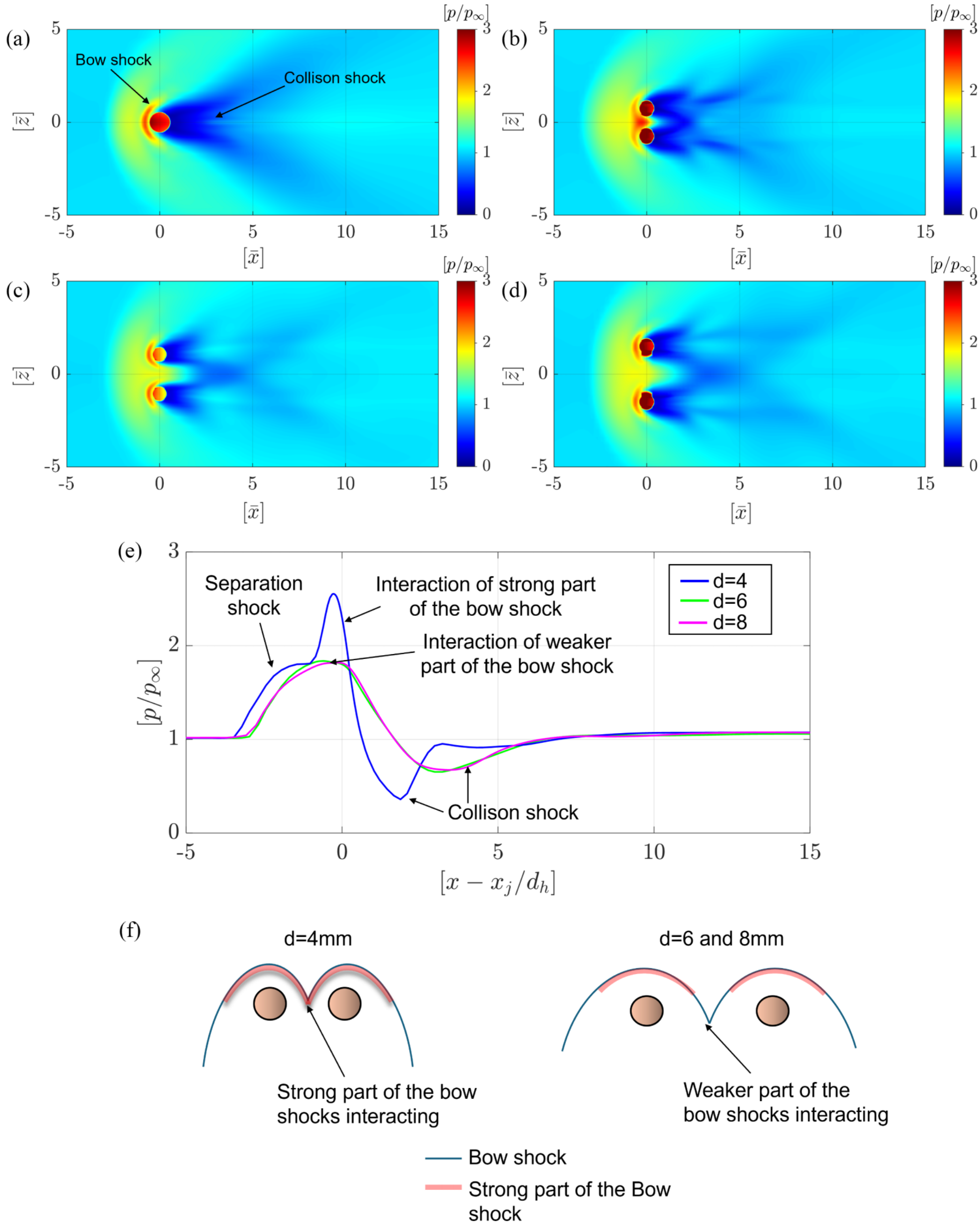

FIG. 15. Contours of wall static pressure nondimensionalized with the freestream pressure for various cases: (a) C-0, (b) C-I, (c) C-II, and (d) C-III. (e) Plot showing the comparison of nondimensionalized wall static pressure variation along the bottom wall centerline for various cases. (f) Schematic showing the interaction of the strong/weak part of the bow shocks for different injector spacing.

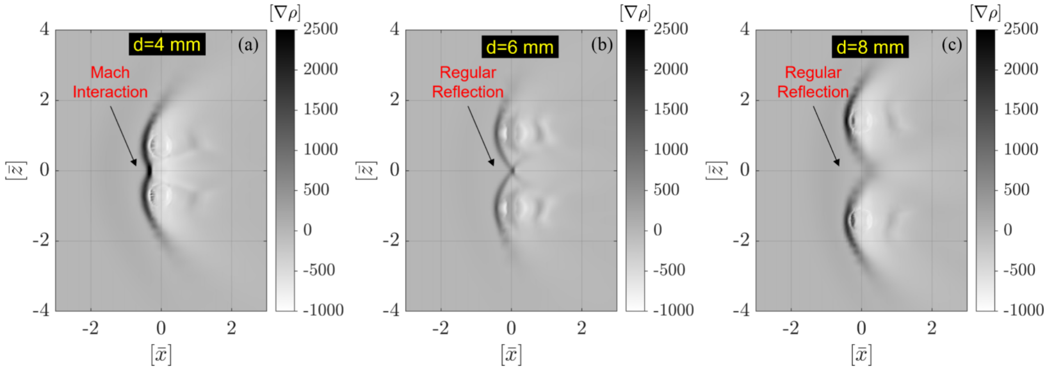

FIG. 16. Contours of density gradient plotted at P_y^3, for various injector spacing cases(a) C-I, (b) C-II, and (c) C-III.

the reattachment of the streamline of the crossflow downstream to the injector. The collision shock can also be observed in the pressure plot as a second peak in the pressure values [Fig. 15(e)].

The shock interactions are further investigated using the numerical schlieren taken at a transverse plane P_y^3, as shown in Fig. 16. It can be seen from Fig. 16(a) that in case C-I, the two bow shock wave interaction leads to a Mach reflection structure, whereas, for larger injector spacing cases (C-II and C-III), the bow shock wave interaction leads to a regular reflection structure, as shown in Figs. 16(b) and 16(c), respectively.

The same results can be observed from the Mach number plot along the duct centerline line ($\bar{z} = 0$) and at a transverse location ($\bar{y} = 1.06$), for various cases of spanwise-tandem injection (C-I to C-III), as shown in Fig. 17(a). For the $d = 4$ mm case, a higher dip in Mach number is observed

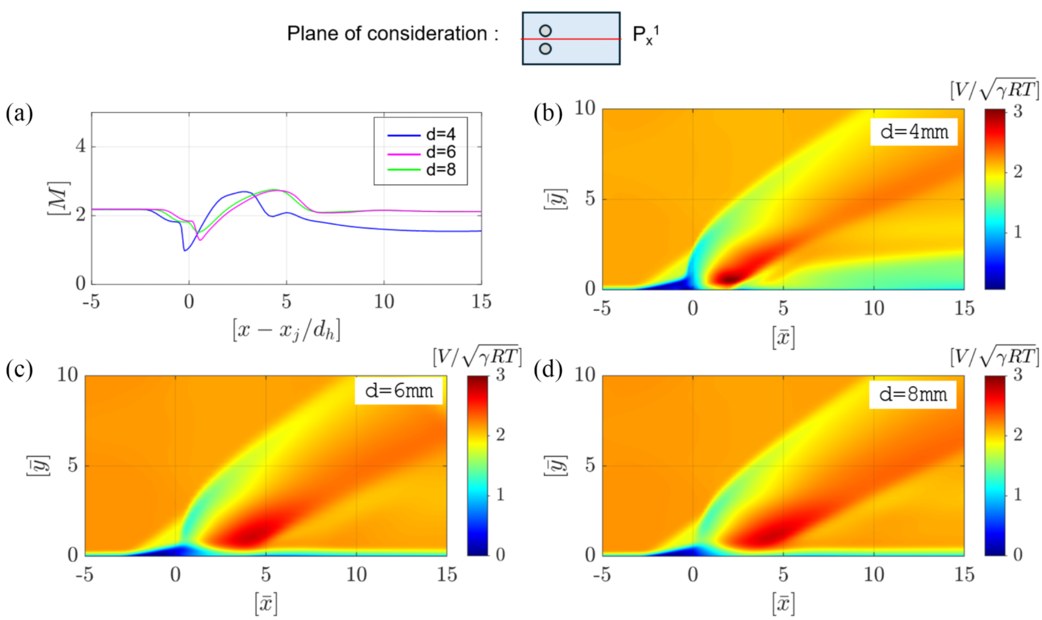

FIG. 17. (a) Mach number variation at the centerline line of the bottom wall [$\bar{y} = 1.06, \bar{z} = 0$]. Contours of Mach number at the streamwise plane located at the centerline of the duct (P_z^1) for various cases: (a) C-0, (b) C-I, and (c) C-II.

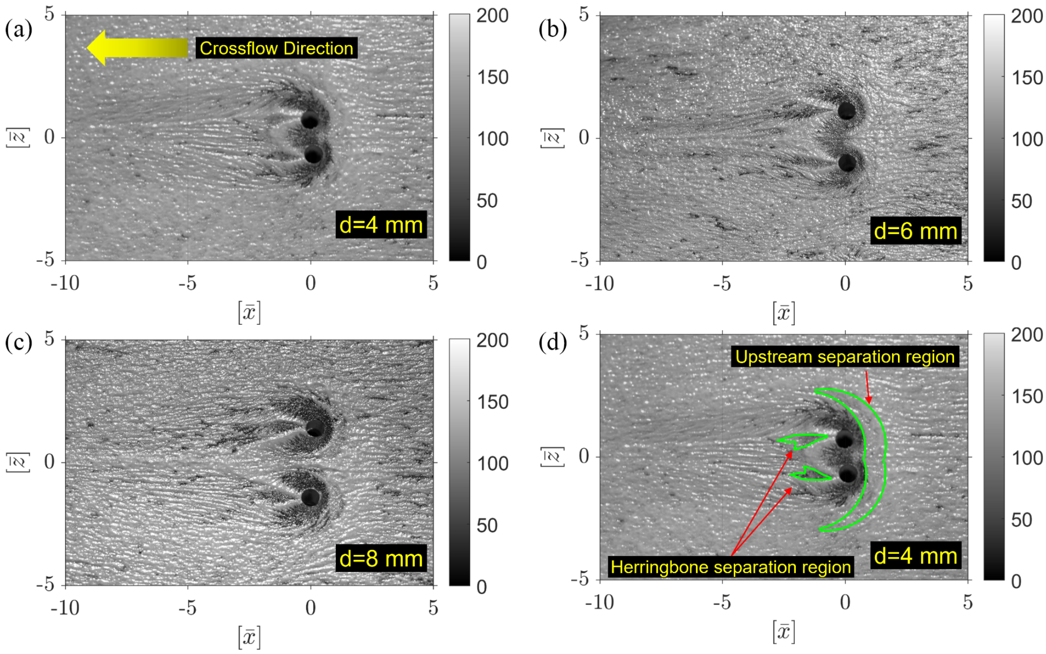

FIG. 18. Images of surface oil flow visualization for various cases: (a) C-I, (b) C-II, (c) C-III, and (d) C-I with separation region demarcated with green lines.

compared to the case with $d = 6$ and 8 mm injector spacings. It can be noted that the Mach number values downstream to the shock interaction for $d = 4$ mm are reaching subsonic values, whereas, for the $d = 6$ and 8 mm cases, it is in the supersonic regime. This also clearly indicates that the strong part of the bow shock waves interacts with each other for the $d = 4$ mm case, whereas for the $d = 6$ and 8 mm cases, the weak part of the bow shock waves interacts. The crossflow, influenced by bow shock wave reflections, further progresses through the interjet spacing region. Here it experiences a subsequent acceleration attributed to the convergent-divergent passage created by the spanwise-tandem injectors. The Mach number contours taken at the duct center plane (P_z^1) also depict similar findings, as shown in Figs. 17(b)–17(d).

3. Flow separation

To analyze the flow separation caused by the interaction of the supersonic crossflow with the two spanwise-tandem jets, surface oil flow visualization was performed on the bottom wall, as shown in Fig. 18. From the oil flow visualization images, it can be seen that the two bow shock waves produced by the injected jets lead to the formation of a separation region upstream of the injectors. The surface oil flow visualization also reveals that there exists a separation region downstream of the injector. Two herringbone-shaped (V-shaped) separation regions downstream of the injector location can be seen from the oil flow visualization (Fig. 18). This is caused by the adverse pressure gradient produced by the collision shock formed due to the reattachment of the supersonic crossflow as it flows around the injected jet and tries to meet downstream to the jet. In the case with $d = 4$ mm (C-I), the separation region formed downstream of the injector is smaller compared to the cases with larger injector spacing (C-II and C-III). This is because, in the case of smaller injector spacing, the collision shocks are formed closer to the injector location, thus creating a smaller separation region. However, in the case of $d = 6$ and 8 mm, the collision shocks are formed at a larger distance from the injector location, which results in the formation of a larger herringbone separation region.

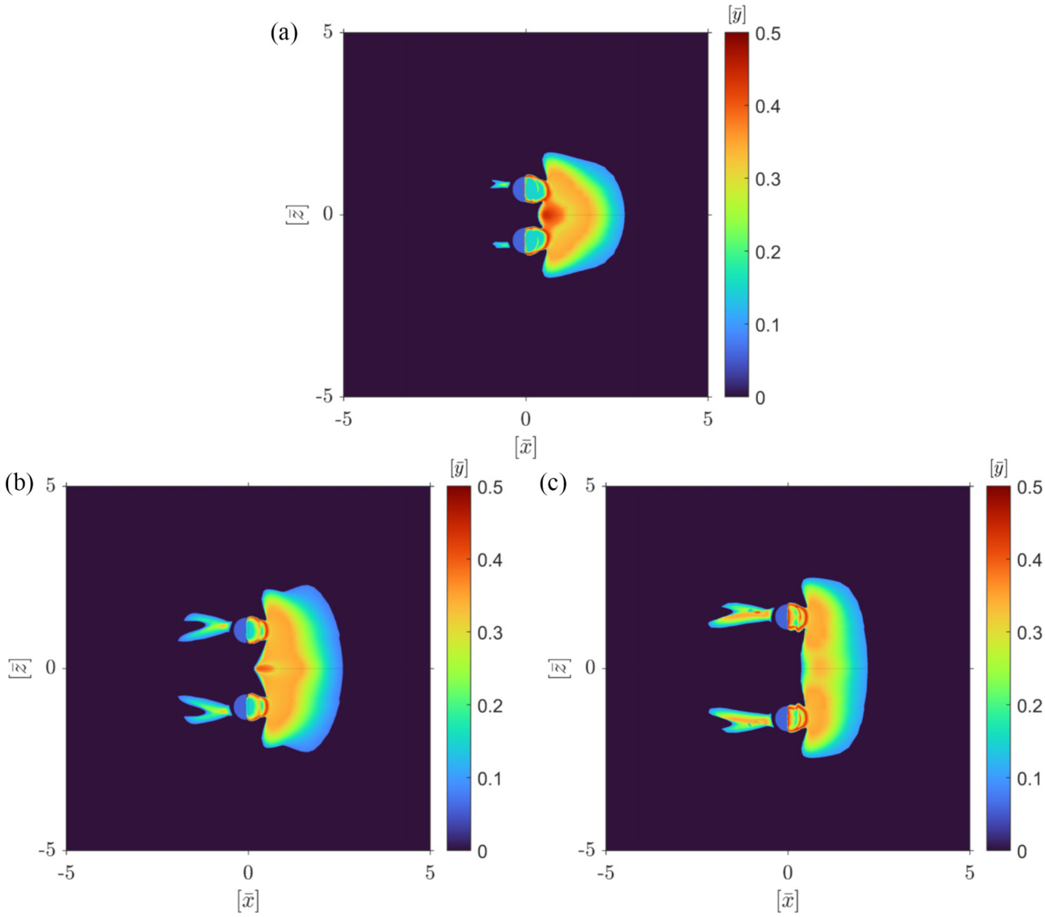

FIG. 19. Isosurfaces of $u/U_\infty = 0$ colored with nondimensionalized transverse distance [$\bar{y}$] for various cases: (a) C-I, (b) C-II, and (c) C-III showing the separation region created by the spanwise tandem injection in a supersonic crossflow.

This can be seen in Fig. 18. The visible outlines of the separation regions are shown in Fig. 18(d). This phenomenon can also be seen from the numerically computed result showing the isosurfaces of nondimensionalized x-velocity component $u/U_\infty = 0$ colored with the nondimensional transverse location ($\bar{y}$), as shown in Fig. 19. The typical separation region upstream to the injector location can be seen. Downstream to the injector, a herringbone-shaped separation region can also be seen due to the collision shock created by the crossflow reattachment.

4. Dominant vortex structures

It is well reported that the transverse injection into supersonic cross-flow results in the roll-up of the injected jet and forming a counter-rotating vortex pair [45]. Additionally, studies indicate that the separated flow induced by the interaction between the bow shock wave and the boundary layer will be carried by the cross-flow, forming a distinctive horseshoe vortex around the injection locations.

The dominant vortex structures for various cases (C-0 to C-III) are identified by computing the iso-surface of the λ_2 criterion, set at a threshold of -7×10^8, as shown in Fig. 20. Figure 20(a) depicts the isosurfaces of λ_2 criterion for the baseline case C-0 (single injector). The λ_2 isosurface shows the formation of the Counter-rotating Vortex Pair (CVP) in the injected jet. Moreover, the

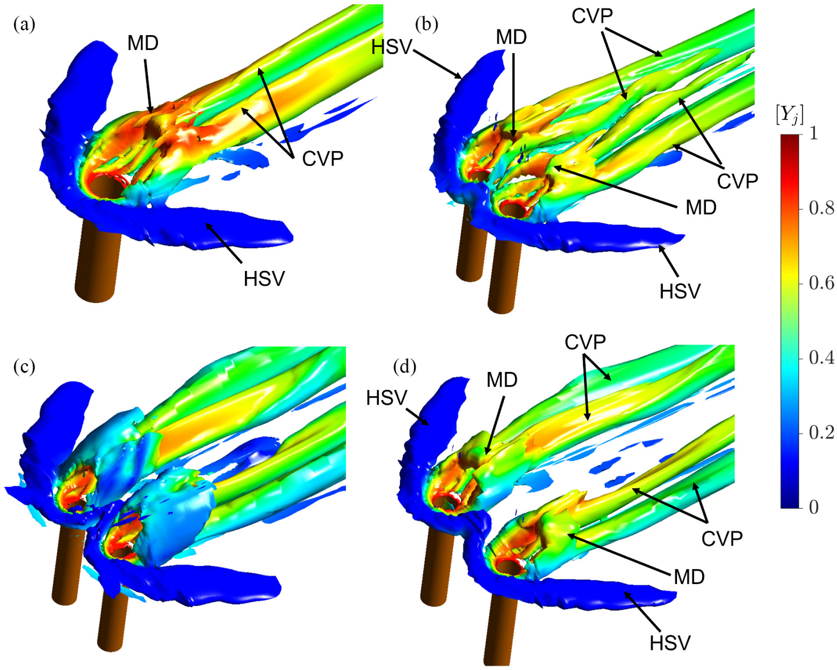

FIG. 20. Isosurfaces of λ-2 criterion with a threshold value of -7×10^8 colored with mass fraction of the injected jet for various cases: (a) C-0, (b) C-I, (c) C-II, and (d) C-III.

presence of a horseshoe vortex, originating upstream of the injector locations due to the separated flow induced by the bow shock, is also observed. In the case of spanwise-tandem injection (C-I, C-II, and C-III), the Lambda 2 criterion discerns two distinct pairs of CVPs, revealing the intricate nature of the flow patterns, as illustrated in Figs. 20(b)–20(d). The $\lambda - 2$ visualization also captures the emergence of two distinct horseshoe vortex regions in the spanwise-tandem injection configuration due to the separate bow shock waves originating from the two distinct injected jets, as shown in Fig. 20. It is also seen from Fig. 20 that the two horseshoe vortices interact with each other for all the spanwise-tandem injection cases (C-I to C-III). These multiple vortices produced by tandem injection configuration will help to improve the mixing characteristics compared to the single injection case. Figure 21 shows the helicity contour at the spanwise plane (P_x^1) for single injection [Fig. 21(a)] and tandem injection [Figs. 21(b) and 21(c)] with various injector spacing (C-0 to C-III). It is seen from the helicity contour that two pairs of CVPs can be seen for the tandem injection cases compared to the single pair of CVPs for the single injection case. In the case of $d = 4$ mm, the CVPs are seen to be closely packed, and therefore, the vorticity zone present at the central region is squeezed together, whereas in the case of $d = 6$ and 8 mm, the vortex pairs are far apart from each other and thus not interacting with each other. It can also be seen that in the case of $d = 8$ mm, the CVPs are pushed outwards in the spanwise direction, as shown in Fig. 21. This is because the large interjet spacing allows the cross-flow to fill the passage area between the two jets and push them sidewards, as discussed earlier in Sec. IV A.

5. Shear layer dynamics and shock oscillation

In the case of a transverse jet in supersonic crossflow, the injected jet and the crossflow are perpendicular to each other. This causes the formation of a skewed shear layer between the injected jet and the crossflow. To investigate the shear layer dynamics, a new set of CFD simulations based on

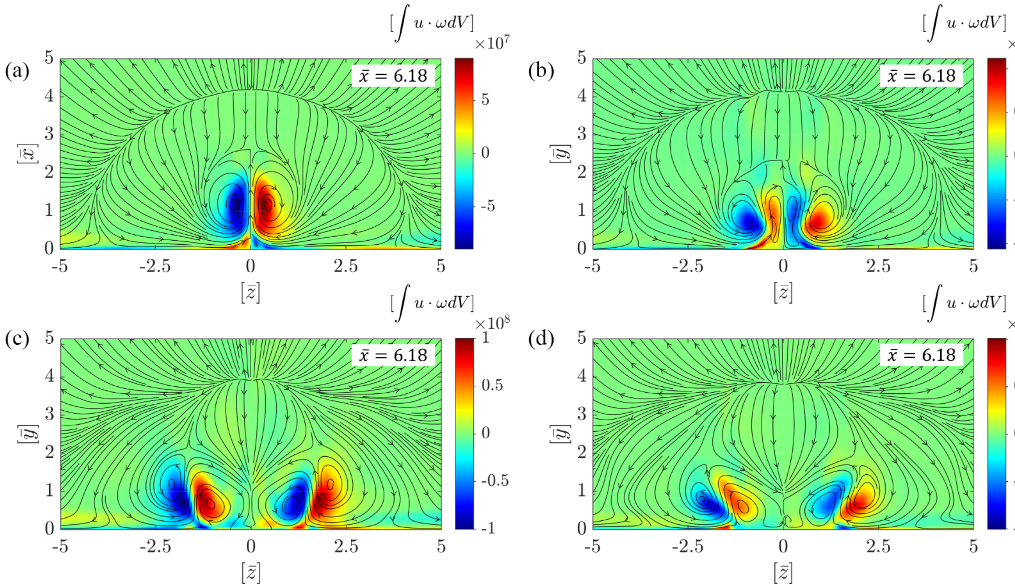

FIG. 21. Helicity contours overlaid with the streamlines at the spanwise plane P_x^1 ($\bar{x} = 6.18$) for various cases: (a) C-0, (b) C-I, (c) C-II, and (d) C-III.

the improved delayed detached eddy simulation (IDDES) turbulence model was performed for case C-I. The IDDES model, a robust approach to turbulence modeling, employs the k-ω SST model to capture near-wall turbulence, while Large Eddy Simulation (LES) is used to model the free-stream region, where large-scale turbulent structures dominate.

First, to investigate the separation characteristics, instantaneous streamlines have been plotted at the plane P_z^2 passing through the center of the first injected jet, as shown in Fig. 22. The instantaneous streamlines clearly show the separation vortex and the hovering vortex upstream to the injected jet. The hovering vortex is produced by the K-H instabilities in the jet shear layer and is the primary cause of the jet instability mechanism prompting the vortex shedding in the injected jet shear layer, as reported by Kelso, Lim, and Perry [46]. To further investigate the vortex shedding patterns, the transient evolution of the mass fraction of the injected jet in the plane P_z^2 obtained from the IDDES simulations has been plotted, as shown in Fig. 23. The mass fraction evolution contours clearly show the unsteady characteristics of the hovering vortex and, consequently, the shear layer vortex formation and its shedding in the injected jet boundary. The oscillation frequency of the shear layer is found from the mass fraction contours by stacking the mass fraction values at a monitoring line corresponding to $[\bar{y} = 0.53]$ over a time of 4 ms, as shown in Fig. 24(a). A fast Fourier transform of this mass fraction distribution along the particular y axis over a time interval (y-t plot) has been computed to find the dominant oscillation frequency, as shown in Fig. 24(b). It is found that the shear layer vortex shedding results in unsteady oscillation of the injected jet shear layer, and the frequency of the jet shear layer oscillation is found to be nearly 363 Hz. The FFT plot also reveals several additional frequency ranges with significantly lower amplitudes. These may represent harmonics of the dominant frequency or could be attributable to computational errors.

Due to the unsteady nature of the jet shear layer oscillation, the bow shock upstream to the individual jets is expected to oscillate. The shock oscillation frequency is also computed by stacking the instantaneous density gradient values along the horizontal line ($\bar{y} = 0.53$) in the plane passing through the center of the injected jet, as shown in Fig. 24(c). A fast Fourier transform of the stacked y-t plot of density gradients has been computed to plot the frequency spectrum of

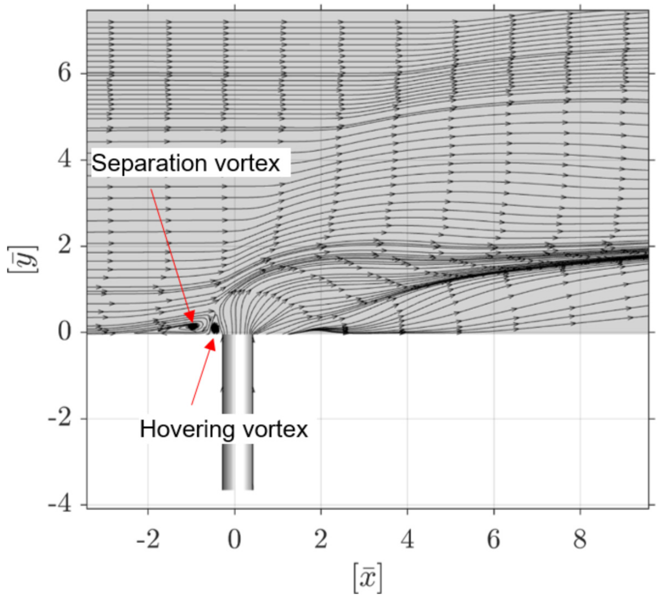

FIG. 22. Projection of instantaneous streamlines in the xy direction, plotted at the plane P_z^2 showing the vortex structures present in the jet shear layer.

the shock oscillation, as shown in Fig. 24(d). It is found that the dominant frequency of shock oscillation (380 Hz) nearly matches the shear layer oscillation frequency, which reveals that the shock oscillations are also caused by the shear layer vortex shedding.

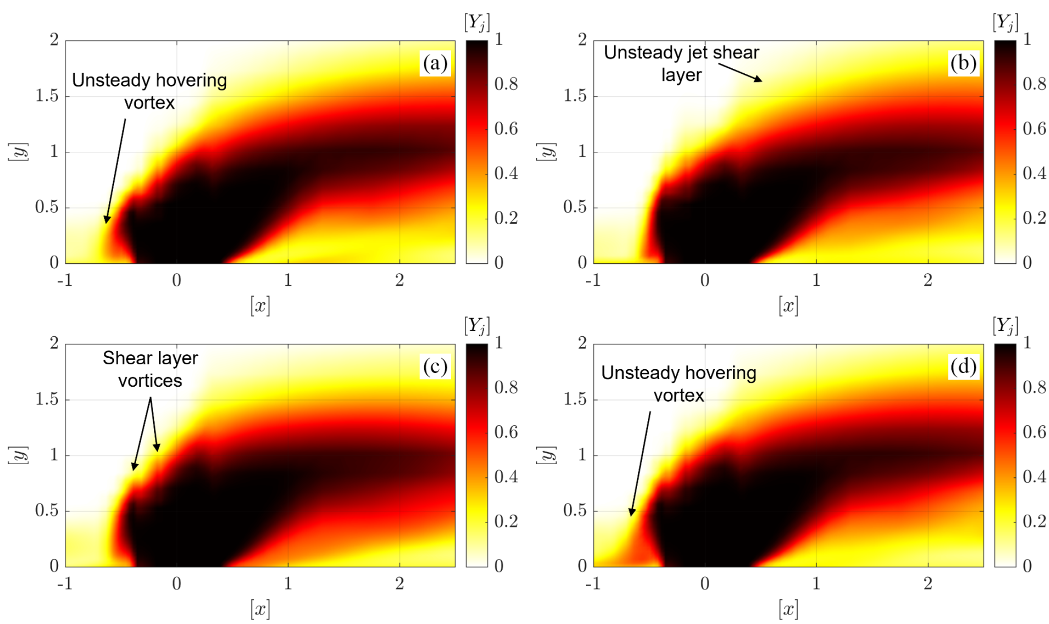

FIG. 23. Transient evolution of the mass fraction of the injected jet showing the unsteady shear layer characteristics for the case C-I at time instance (a) $t = 0$ ms, (b) $t = 50$ ms, (c) $t = 100$ ms, and (d) $t = 150$ ms.

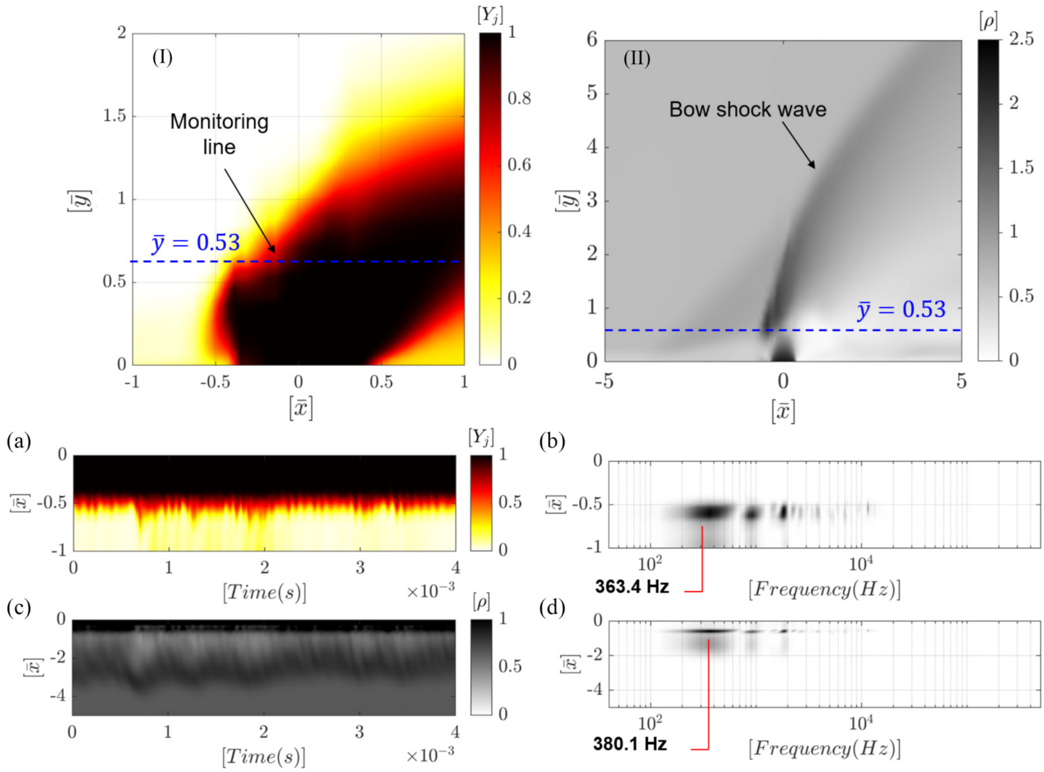

FIG. 24. A zoomed view of the contour of the (I) mass fraction and (II) Density at $[\bar{x} = 0]$ for the case C-I. (a) *x*-*t* plot showing the stacked mass fraction values taken at $\bar{y} = 0.53$. (b) FFT of the corresponding mass fraction *x*-*t* plot. (c) *x*-*t* plot showing the stacked density values taken at $\bar{y} = 0.53$. (d) FFT of the corresponding density *x*-*t* plot.

In the present study, an attempt was made to investigate the unsteady shear layer vortices and jet oscillations using PLMS-based flow visualization experiments. However, the PLMS imaging was conducted with a continuous laser of 0.5 W power. Due to the low power of the continuous laser, capturing highly time-resolved, sharp images was challenging. Consequently, the current PLMS experiments could not resolve the shear layer vortices due to limitations in laser power and synchronized high-speed imaging. Despite these limitations, the PLMS images obtained in this study successfully captured jet penetration, which was the primary focus of the flow visualization study. To investigate the shear layer vortices, CFD simulations using the IDDES model were utilized.

B. Mixing characteristics

The mixing characteristics are evaluated by investigating the jet penetration in the transverse direction and the jet spread in the spanwise direction, as well as by computing the mixing efficiency.

1. *Jet penetration*

The penetration characteristics of spanwise tandem injection jets have been investigated using experimental and numerical methods. Experimental penetration data for spanwise tandem injection were obtained through Planar Laser-Based Mie Scattering (PLMS) images at the injector center plane (P_z^2) for different cases (C-0 to C-III), as shown in Figs. 25(b)–25(e). Quantitative penetration

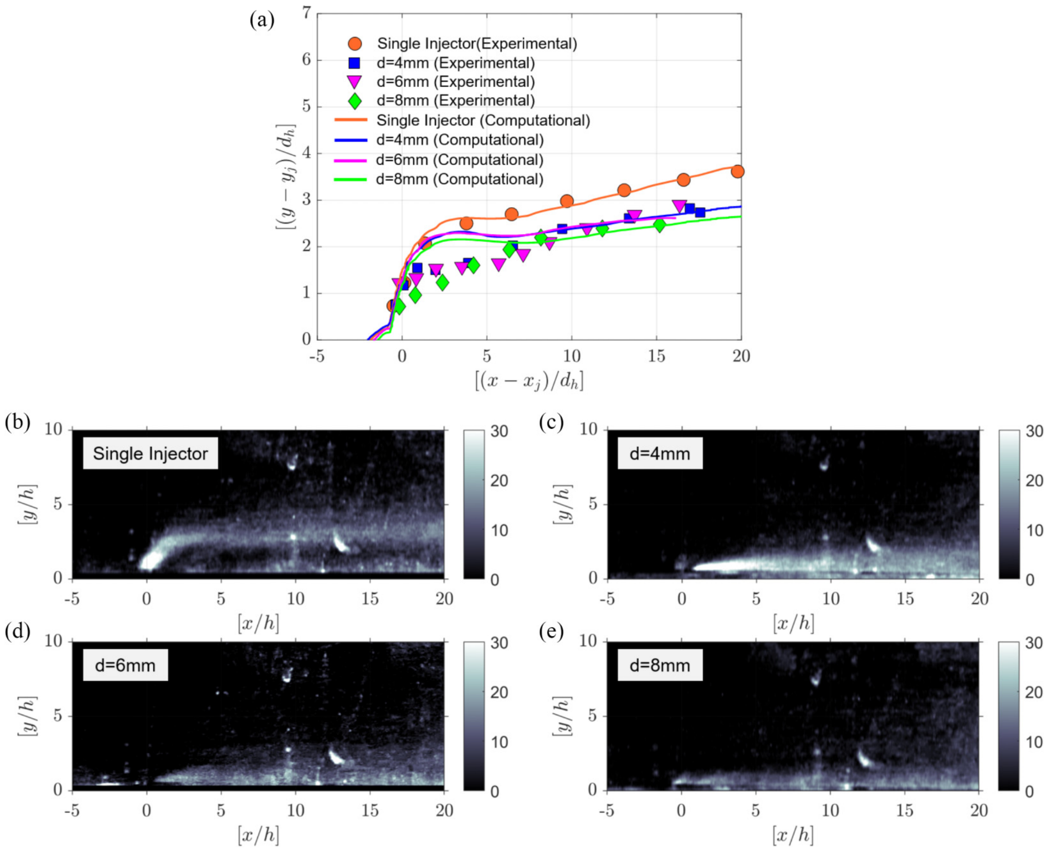

FIG. 25. (a) Comparison of numerical and experimental transverse penetration of the injected jet in the supersonic crossflow for various cases. PLMS images captured at the plane P_z^2 for various cases: (b) C-0, (c) C-I, (d) C-II, and (e) C-III.

values from planner laser-based Mie scattering images were determined by plotting the locus of the transverse locations where the scattered light intensity reaches 10% of the maximum value. For the computational study, the jet penetration has been determined by plotting the locus of points in the transverse direction where the mass fraction of the injected jet reaches 10% ($Y_j = 0.1$). For all the cases, the jet penetration is computed at the plane P_z^2. The comparison of the experimentally measured and computationally predicted jet penetration in the transverse direction shows a close match, as shown in Fig. 25(a). It is seen that the experimental and computational penetration data show a slight mismatch closer to the injection location ($\bar{x} = 1$ to $\bar{x} = 5$). This might be due to the fact that the current turbulence modeling is underpredicting the high shear region near the injector location. Moreover, the slight vibration in the test section will lead to minor errors in the jet boundary prediction. Figure 25 shows that the baseline circular jet exhibited greater penetration compared to the spanwise tandem injection cases(C-I to C-III). This is due to the higher mass flow rate injected by the baseline with a single circular orifice compared to the injected mass flow rate from the individual jet in the spanwise tandem injection. The jet penetration for a single injector case (C-0) predicted from the present study is compared with the penetration correlations reported previously. In these studies, a generic correlation, as shown in Eq. (3), was used to find the penetration for a single injected jet case:

$$P/D = A(q_j/q_a)^B (x/D + C)^E (\delta/d_h)^F (M_j/M_a)^G. \tag{3}$$

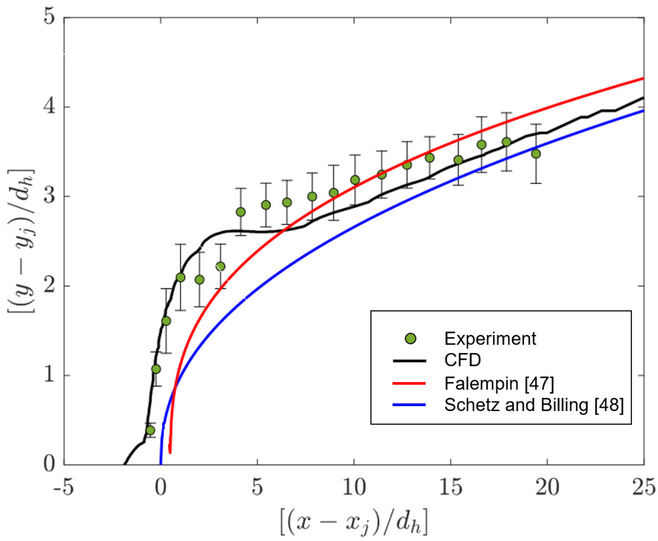

FIG. 26. Comparison of jet penetration obtained from the computations, experiments, and different correlations [47,48].

Here q_j and q_a are the momentum fluxes of the jet and the crossflow, δ is the boundary layer thickness, and M_j and M_a are the Mach number of the jet and the crossflow. The various past studies on the jet penetration correlation investigated the effect of coefficients in optimizing the model's accuracy. Figure 26 compares the penetration obtained from computations, experiments, and correlation with different coefficients identified in the previous studies [47,48]. It can be seen that the penetration values obtained from the present study match closely the previously used correlation equations.

2. Experimental spanwise jet spread efficiency

The spanwise spread of the injected jet for various cases (C-0 to C-III) has been evaluated using time-averaged PLMS images captured at the plane P_x^1 (see Fig. 5), as shown in Fig. 27. The pixel intensity of the images is normalized (using Gaussian normalization) and transformed into contours using MATLAB® software. A qualitative examination of the Mie scattering images shows that for the single injector case (C-0), the scattered light intensity is higher in the jet core region compared to the spanwise tandem injection cases (C-I to C-III). This is attributed to the higher concentration of the seeding particle injected from the single injector compared to spanwise tandem injectors. This demonstrates that the seeder particles remain unmixed in the core region for the single injector case, whereas the seeder particles injected from the spanwise tandem injectors get mixed properly with the crossflow. This is because, in the case of a single injector, the entire mass flow is injected from a single orifice having a higher diameter, which results in a higher concentration of seeder particles in the jet core region, thereby delaying the mixing processes significantly. In contrast, the mass injected from the spanwise tandem injectors is distributed into two injectors (having smaller diameters), resulting in the spreading of the seeding particle, which augments the mixing process significantly.

Consequently, an experimental spread efficiency (ζ_m) has been determined from PLMS images for various cases, as shown in Fig. 27(e). In order to quantify ζ_m, a threshold value of the normalized scattered light intensity of $I_s = 0.25$ is arbitrarily chosen. If the normalized light intensity value at a particular pixel is lower than the threshold value (I_s), the injected jet is inferred to be completely mixed with the crossflow. Conversely, if the normalized light intensity value is greater than the threshold value, then a portion of the injected jet is inferred to be mixed with the crossflow

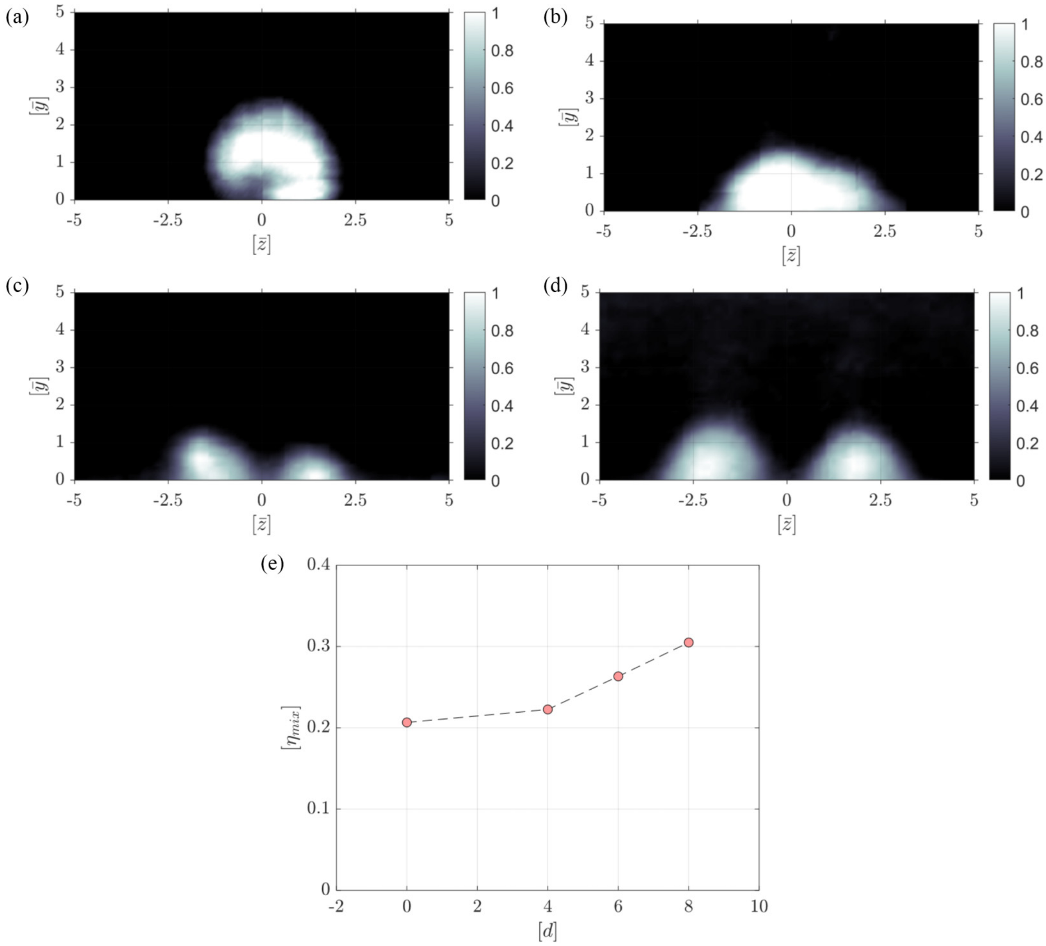

FIG. 27. Planar laser-based Mie scattering images taken at a plane P_x^1 for various cases: (a) C-0, (b) C-I, (c) C-II, (d) C-III, and (e) plot showing the comparison of experimental mixing efficiency for various cases.

(improperly mixed). A comprehensive discussion of the methodology to evaluate the jet spread efficiency is provided in the Appendix. It can be seen from Fig. 27(e) that ζ_m for the baseline case is lower compared to the spanwise tandem injection cases. This is caused by the higher jet concentration of the injected jet fluid in the baseline case (C-0) compared to the spanwise tandem injectors. Moreover, the value of ζ_m in the case of spanwise tandem injection increases as the injector spacing increases. This is because, in the case of spanwise tandem injection with $d = 4$ mm, the two injectors are placed closer to each other, which results in significant jet-jet interactions. This lowers the jet spread and hence shows a lower ζ_m value. In the case of injector spacing with $d = 6$ and 8 mm (C-II and C-III), the injector spacing is large enough to cause lesser interjet interaction, thus creating a larger spread of the jet and having higher spread efficiency.

3. Computational mixing efficiency

In the present study, the computationally determined mixing efficiency (η_m) is evaluated for various cases (C-0 to C-III), and a comparison is made with the baseline case (C-0), as shown in Fig. 28. Mixing efficiency (η_m)is defined as the ratio between the mass of the injected jet (simulating the fuel available for combustion) and the total injected mass ($\dot{m}_{\text{total}}$), as defined in Eq. (4) [49]. The

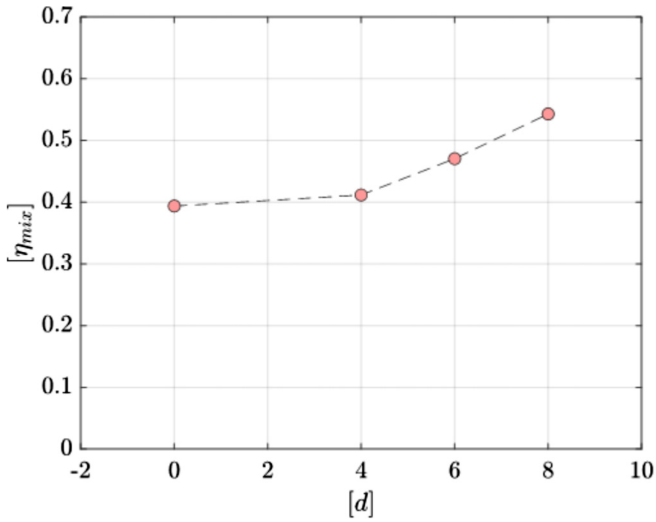

FIG. 28. Variation of computational mixing efficiency for various injector spacing cases: C-0 to C-III. For a stoichiometric mass fraction value ($\alpha_s = 0.25$).

mass available for combustion, or the reacted mass flow rate ($\dot{m}_{\text{react}}$), is identified as the overall fuel mass capable of undergoing combustion with the supplied freestream air. To further define the reacted mass flow rate ($\dot{m}_{\text{react}}$), the reacted mass fraction (Y_r) is introduced, representing the proportion of mass fraction that has undergone combustion, while Y_j denotes the total mass fraction, as shown in Eq. (4). Local fluid density (ρ) and the x component of velocity (u) are also considered in the formulation. The reacted mass fraction of the injected jet, Y_r, is detailed in Eq. (A1), where Y_s represents the stoichiometric mass fraction necessary for combustion. Notably, in this study, actual combustion is not taking place, rendering the stoichiometric ratio undefined. Nevertheless, for comparative purposes across various spanwise-tandem injections with a circular injector, a reference stoichiometric ratio of 0.25 is adopted for calculations.

It can be observed from Fig. 28 that the η_m value for the baseline case is lower compared to the spanwise tandem injection cases. This is due to the higher jet concentration of the injected fluid in the baseline case (C-0) compared to the spanwise tandem injectors. Additionally, η_m increases with larger injector spacings in the spanwise tandem injection cases. Specifically, with an injector spacing of $d = 4$ mm (C-I), the injectors are closer together, leading to significant jet-jet interactions. This interaction reduces the jet spread and results in a lower η_m value. In contrast, with injector spacings of $d = 6$ mm (C-II) and $d = 8$ mm (C-III), the increased spacing reduces jet interactions, allowing for a greater jet spread and, consequently, a higher η_m value:

$$\mu_m = \frac{\dot{m}_{\text{mix}}}{\dot{m}_{\text{total}}} = \frac{\int_A Y_R \rho u \, dA}{\int_A Y_j \rho u \, dA}, \tag{4}$$

where

$$Y_R = \begin{cases} Y, & \text{if } Y_j \leqslant Y_S \\ \frac{1-Y}{1-Y_S} Y_S, & \text{if } Y_j \geqslant Y_S \end{cases}. \tag{5}$$

4. *Effect of threshold values of I_s and Y_s on the mixing efficiencies*

Figure 29(a) shows the variation of spread efficiency ζ_m with varying threshold light intensity (I_s)taken from the PLMS images for different injector spacing cases. It is seen that the spread efficiency increases with an increase in the threshold light intensity. This is because, as the threshold

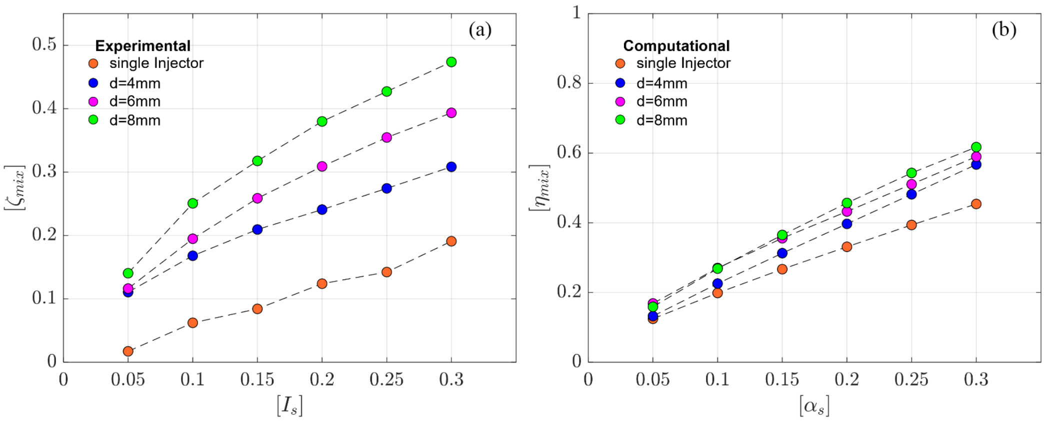

FIG. 29. (a) Variation of experimental spread efficiency (ζ_m) with different threshold light intensity values (I_s) and (b) variation of computational mixing efficiency (η_m) with different threshold light intensity values (α_s).

light intensity increases, the pixels with higher light intensity are also permitted to be considered completely mixed with the freestream. Therefore, the number of pixels falling under the completely mixed regime increases, increasing the spread efficiency.

Figure 29(b) shows the variation of computationally obtained mixing efficiency with varying stoichiometric mass fraction (Y_s) for different injector spacing cases. It can be seen that with an increase in the Y_s value, the mixing efficiency increases. This is because, as the Y_s value increases, the regions with higher injected jet mass fraction (Y) values are also considered to be in the completely mixed regions, thus increasing the mixing efficiency. Additionally, it is seen that at any given Y_s value, the mixing efficiency of all the spanwise tandem injection cases is greater than the single injector case. This is caused by the larger spanwise spread of the injected jet. Moreover, in cases of spawnwise tandem injection, it is seen that with the increase in injector spacing, the mixing efficiency increases.

It should be noted that even though the methodology used to calculate η_m and ζ_m are similar, the resulting values might differ. However, the trends observed will remain consistent. For evaluating mixing efficiency (η_m) using the computations, the variables considered include mass fraction, fluid density, and axial velocity. In contrast, the calculation of spread efficiency (ζ_m) relies solely on light intensity. Since light intensity does not directly correspond to the variables used for η_m, the values for ζ_m may not be directly comparable to those for η_m.

V. CONCLUSION

The present study investigates the interaction of two spanwise tandemly injected jets with a supersonic crossflow using experimental and computational techniques. The study also investigates the effect of injector spacing on the flow field flow and mixing characteristics. It is seen from the mass fraction distribution of the injected jet that in the case of smaller injector spacing ($d = 4$ mm), the jets interact with each other, which leaves a lesser interjet passage gap. This causes lesser entertainment of the supersonic crossflow from the top. In contrast, for larger injector spacing, the supersonic crossflow is easily entrained, and the mixing process is more prevalent. It is also observed that the supersonic crossflow initially decelerates and then accelerates as it flows through the interjet passage space. For tandem injection cases, separate bow shock waves are produced by the individual jets, which interact with each other at the center plane. It is seen that, in the case of lower injector spacing, the strong part of the bow shocks interact, resulting in deceleration of the crossflow to a subsonic flow. On the other hand, for larger injector spacing, the weak part of the bow shock waves interact with each other, which results in the flow getting decelerated to a low supersonic flow. The strong interaction of the two bow shocks in the smaller injector spacing cases causes a larger separation region upstream of the injectors. Surface oil flow visualization and isosurfaces of $u/U_\infty = 0$ revealed the presence of two herringbone-shaped separation regions downstream to the injector locations, which are formed due to the collision shocks. The isosurface of $\lambda - 2$ criterion revealed the presence of various vortex patterns, such as the horseshoe vortex and the CVPs. The nature of the two contour-rotating vortex pairs (one from each jet) is further analyzed using helicity contours at a downstream cross-stream plane. It is seen that for smaller injector spacing, the CVPs interact with each other, and in larger injector spacing, the CVPs are pushed outward due to the larger momentum of the crossflow interacting with the injected jet. The mixing characteristics investigated using Mie scattering reveal that with an increase in injector spacing, the mixing efficiency increases significantly. The penetration of the injected jet in the spanwise-tandem injection cases is found to be lower than in the single injector case.

APPENDIX: ESTIMATION OF EXPERIMENTAL SPREAD EFFICIENCY

In the present study, the experimental spread efficiency is determined using the PLMS images taken at a spanwise plane (P_x^1). A sequence of images (200 samples) is time-averaged using MATLAB, and the time-averaged image is normalized using Gaussian normalization and converted into contours. Here the normalized scattered light intensity from the olive oil particles is treated analogously to the injected jet mass fraction.

The spread efficiency is defined as the ratio of the number of pixels designating the proper mixing of the fuel with the air ($Area_{\text{mix}}$) to the total number of pixels in a fixed area ($Area_{\text{total}}$), as shown in Eq. (A1). Here $Area_{\text{mix}}$ is further defined based on a threshold normalized intensity value of $I_s = 0.25$. If the normalized pixel intensity at a particular location ($I_{(i,j)}$) is found to be $\leqslant 0.25$, then the injected jet is considered to have a complete mixing of all the particles in that pixel area. If the normalized pixel intensity at any location ($I_{(i,j)}$) is $\geqslant 0.25$, then the injected jet is considered to be mixed partially, which is further given in Eq. (A2).

Figures 30(a) and 30(b) show the PLMS image for a single injector case (C-0) taken at plane P_x^1 showing partially mixed pixels (red dots) and properly mixed pixel (yellow dots)

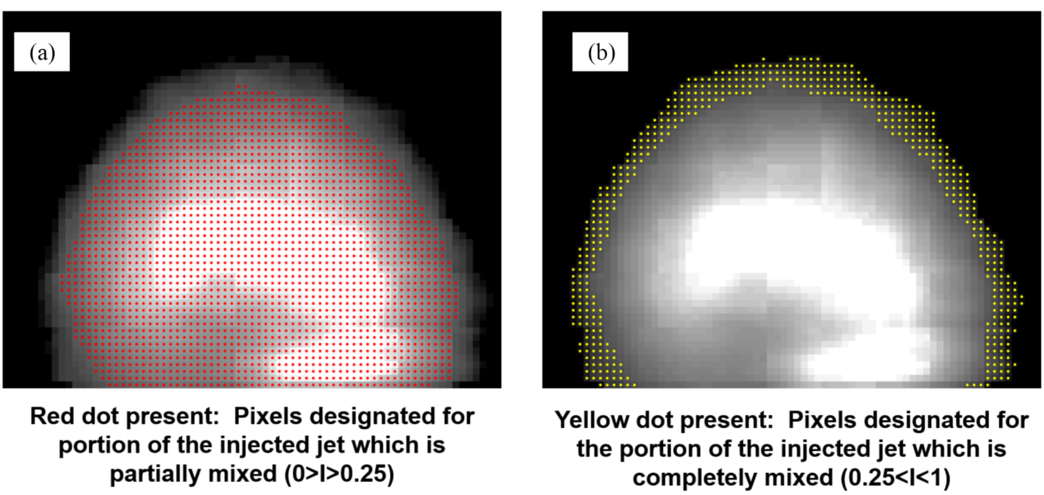

FIG. 30. PLMS images for the single injector case. (a) Pixels with red dots representing partially mixed regions (b) Pixels with yellow dots representing the completely mixed region.

respectively:

$$\zeta_m = \frac{\text{Area}_{\text{mix}}}{\text{Area}_{\text{total}}} = \frac{\int_A I_{\text{mix}}\, dA}{\int_A I_{(i,j)}\, dA}, \tag{A1}$$

where

$$I_{\text{mix}} = \begin{cases} I_{(i,j)}, & \text{if } I_{(i,j)} \leqslant I_s \\ \frac{1-I_{(i,j)}}{1-I_s} I_s, & \text{if } I_{(i,j)} \geqslant I_s \end{cases}. \tag{A2}$$

This definition of partially mixed regions is analogous to the mixing efficiency in the reported case of two combustible species [49]. This work described mixing efficiency as a ratio of the total fuel that participates in combustion ($\dot{m}_{\text{mix}}$) to the total fuel injected ($\dot{m}_{\text{total}}$). The amount of fuel participating in combustion is calculated by considering the stoichiometric ratio of the fuel. If the mass fraction (α) of the fuel at a particular location is less than or equal to the stoichiometric mass fraction α_s then the fuel is considered to burn completely. Furthermore, if the mass fraction of the fuel is greater than the stoichiometric mass fraction, then the fuel is considered to be partially burnt, as shown in Eq. (A3) and Eq. (A4). Here ρ is the density of the mixture at a particular location, u is the axial velocity, and α_R is the mass fraction that participated in the combustion process:

$$\mu_m = \frac{\dot{m}_{\text{mix}}}{\dot{m}_{\text{total}}} = \frac{\int_A \alpha_R \rho u\, dA}{\int_A \alpha \rho u\, dA}, \tag{A3}$$

where

$$\alpha_R = \begin{cases} \alpha, & \text{if } \alpha \leqslant \alpha_S \\ \frac{1-\alpha}{1-\alpha_S} \alpha_S, & \text{if } \alpha \geqslant \alpha_S \end{cases}. \tag{A4}$$

In the present study, instead of the mass fraction of the injected jet, the light intensity is considered for evaluating the spread efficiency. However, density and axial velocity are not considered, as they are challenging to measure in the experiments. Instead of a stoichiometric ratio, a threshold scattered light intensity value is chosen ($I_s = 0.25$). This threshold value is purely arbitrary. Nevertheless, this will give a good comparison of the spread efficiency for various cases.

[1] X. Chai, P. S. Iyer, and K. Mahesh, Numerical study of high speed jets in crossflow, J. Fluid Mech. **785**, 152 (2015).

[2] S. Kawai and S. K. Lele, Large-eddy simulation of jet mixing in supersonic crossflows, AIAA J. **48**, 2063 (2010).

[3] F. Génin and S. Menon, Dynamics of sonic jet injection into supersonic crossflow, J. Turbul. **11**, N4 (2010).

[4] Z. A. Rana, B. Thornber, and D. Drikakis, Transverse jet injection into a supersonic turbulent cross-flow, Phys. Fluids **23**, 046103 (2011).

[5] M.-B. Sun and Z.-W. Hu, Mixing in nearwall regions downstream of a sonic jet in a supersonic crossflow at Mach 2.7, Phys. Fluids **30**, 106102 (2018).

[6] A. Ben-Yakar, M. Mungal, and R. Hanson, Time evolution and mixing characteristics of hydrogen and ethylene transverse jets in supersonic crossflows, Phys. Fluids **18**, 026101 (2006).

[7] M. R. Gruber, A. Nejad, T. Chen, and J. C. Dutton, Compressibility effects in supersonic transverse injection flowfields, Phys. Fluids **9**, 1448 (1997).

[8] D. Papamoschou and D. Hubbard, Visual observations of supersonic transverse jets, Exp. Fluids **14**, 468 (1993).

[9] S. L. N. Desikan and J. Kurian, Strut-based gaseous injection into a supersonic stream, J. Propul. Power **22**, 474 (2006).

[10] Y. Jiang, N. H. Abu-Hamdeh, R. A. Bantan, and Z. Li, Influence of upstream angled ramp on fuel mixing of hydrogen jet at supersonic cross flow, Aerosp. Sci. Technol. **119**, 107099 (2021).
[11] R. Balar, K. Yu, A. Gupta, and A. Kothari, Pylon-aided fuel injection into supersonic flow, in *Proceedings of the 45th AIAA Aerospace Sciences Meeting and Exhibit* (AIAA Press, Reston, VA, 2007), p. 834.
[12] Y. Liu, M. B. Sun, C. H. Liang, J. F. Yu, and G. X. Li, Flowfield structures of pylon-aided fuel injection into a supersonic crossflow, Acta Astronaut. **162**, 306 (2019).
[13] A. Oamjee and R. Sadanandan, Fuel injection location studies on pylon-cavity aided jet in supersonic crossflow, Aerosp. Sci. Technol. **92**, 869 (2019).
[14] M. R. Gruber, C. D. Carter, D. R. Montes, L. C. Haubelt, P. I. King, and K.-Y. Hsu, Experimental studies of pylon-aided fuel injection into a supersonic crossflow, J. Propul. Power **24**, 460 (2008).
[15] M. Vishwakarma and A. Vaidyanathan, Experimental study of mixing enhancement using pylon in supersonic flow, Acta Astronaut. **118**, 21 (2016).
[16] A. Ben-Yakar and R. Hanson, Cavity flameholders for ignition and flame stabilization in scramjets-Review and experimental study, in *Proceedings of the 34th AIAA/ASME/SAE/ASEE Joint Propulsion Conference and Exhibit* (AIAA Press, Reston, VA, 1998), p. 3122.
[17] A. Ben-Yakar and R. Hanson, Supersonic combustion of cross-flow jets and the influence of cavity flame-holders, in *Proceedings of the 37th Aerospace Sciences Meeting and Exhibit* (AIAA Press, Reston, VA, 1999), p. 484.
[18] S. Desikan, S. Pandian, P. P. Simha, and N. Sahoo, Experiments on flow past cavity and the application of modal decomposition techniques, Eur. J. Mech. B Fluids **94**, 293 (2022).
[19] S. K. Karthick, Shock and shear layer interactions in a confined supersonic cavity flow, Phys. Fluids **33**, 066102 (2021).
[20] B. Parent, J. P. Sislian, and J. Schumacher, Numerical investigation of the turbulent mixing performance of a cantilevered ramp injector, AIAA J. **40**, 1559 (2002).
[21] Y. Zhang, W. Liu, and M. Sun, Effect of microramp on transverse jet in supersonic crossflow, AIAA J. **54**, 4043 (2016).
[22] C. Aguilera and K. H. Yu, Supersonic mixing enhancement using fin-guided fuel injection, J. Propul. Power **31**, 1532 (2015).
[23] L.-Q. Li, W. Huang, and L. Yan, Mixing augmentation induced by a vortex generator located upstream of the transverse gaseous jet in supersonic flows, Aerosp. Sci. Technol. **68**, 77 (2017).
[24] H. Shi, G. Wang, X. Luo, J. Yang, and X.-Y. Lu, Large-eddy simulation of a pulsed jet into a supersonic crossflow, Comput. Fluids **140**, 320 (2016).
[25] M. Zhao and T. Ye, Urans study of pulsed hydrogen jet characteristics and mixing enhancement in supersonic crossflow, Int. J. Hydrogen Energy **44**, 20493 (2019).
[26] R. T. M'Closkey, J. M. King, L. Cortelezzi, and A. R. Karagozian, The actively controlled jet in crossflow, J. Fluid Mech. **452**, 325 (2002).
[27] S. Maikap, R. Arun Kumar, and H. B. Kothadia, Active flow control of supersonic jet using streamwise pulsed blowing, AIAA J. **60**, 5150 (2022).
[28] S. Maikap, S. K. Karthick, and A. K. Rajagopal, On the flow unsteadiness and operational characteristics of a novel supersonic fluidic oscillator, Phys. Fluids **35**, 096105 (2023).
[29] S. Raghu, Fluidic oscillators for flow control, Exp. Fluids **54**, 1455 (2013).
[30] A. Suresh and A. K. Rajagopal, An active mixing enhancement technique in supersonic ejectors using pulsed streamwise injections, Phys. Fluids **35**, 076111 (2023).
[31] F. Ostermann, R. Woszidlo, C. N. Nayeri, and C. O. Paschereit, The interaction between a spatially oscillating jet emitted by a fluidic oscillator and a cross-flow, J. Fluid Mech. **863**, 215 (2019).
[32] S. Maikap and A. K. Rajagopal, Mixing enhancement of transverse jets in supersonic crossflow using an actively controlled novel fluidic oscillator, Phys. Fluids **36**, 026106 (2024).
[33] H. Takahashi, S. Ikegami, G. Masuya, and M. Hirota, Extended quantitative fluorescence imaging for multicomponent and staged injection into supersonic crossflows, J. Propul. Power **26**, 798 (2010).
[34] S.-H. Lee, Characteristics of dual transverse injection in scramjet combustor, Part 1: Mixing, J. Propul. Power **22**, 1012 (2006).

[35] S.-H. Lee, Characteristics of dual transverse injection in scramjet combustor, Part 2: Combustion, J. Propul. Power **22**, 1020 (2006).
[36] S. Hollo, J. McDaniel, and R. O. Y. Hartfield, Jr., Characterization of supersonic mixing in a nonreacting mach 2 combustor, in *Proceedings of the 30th Aerospace Sciences Meeting and Exhibit* (AIAA Press, Reston, VA, 1992), p. 93.
[37] M. Y. Ali and F. Alvi, Jet arrays in supersonic crossflow—An experimental study, Phys. Fluids **27**, 126102 (2015).
[38] R. Sebastian and A.-M. Schreyer, Influence of jet spacing in spanwise-inclined jet injection in supersonic crossflow, J. Fluid Mech. **946**, A39 (2022).
[39] J. John and T. Keith, *Gas Dynamics* (Pearson Prentice Hall, New York, 2006).
[40] Y. Bartosiewicz, Z. Aidoun, P. Desevaux, and Y. Mercadier, CFD-experiments integration in the evaluation of six turbulence models for supersonic ejectors modeling, in *Integrating CFD and Experiments Conference* (Academia Press, San Francisco, CA, 2003).
[41] J. Kolář and V. Dvořák, Verification of k-ω SST turbulence model for supersonic internal flows, Int. J. Mech. Mechatron. Eng. **5**, 1715 (2011).
[42] M. B. Sun and Z. W. Hu, Generation of upper trailing counter-rotating vortices of a sonic jet in a supersonic crossflow, AIAA J. **56**, 1047 (2018).
[43] Y. Liu, M.-B. Sun, C.-H. Liang, Z. Cai, and Y.-N. Wang, Structures of near-wall wakes subjected to a sonic jet in a supersonic crossflow, Acta Astronaut. **151**, 886 (2018).
[44] C.-H. Liang, M.-B. Sun, Y. Liu, and Y.-X. Yang, Shock wave structures in the wake of sonic transverse jet into a supersonic crossflow, Acta Astronaut. **148**, 12 (2018).
[45] M. Sun and Z. Hu, Formation of surface trailing counter-rotating vortex pairs downstream of a sonic jet in a supersonic cross-flow, J. Fluid Mech. **850**, 551 (2018).
[46] R. M. Kelso, T. Lim, and A. Perry, An experimental study of round jets in cross-flow, J. Fluid Mech. **306**, 111 (1996).
[47] F. H. Felempin, Scramjet developments in France, in *Scramjet Propulsion* (AIAA Press, Reston, VA, 2014), pp. 47–117.
[48] J. A. Schetz and F. S. Billig, Penetration of gaseous jets injected into a supersonic stream. J. Spacecr. Rockets **3**, 1658 (1966).
[49] P. Danckwerts, The definition and measurement of some characteristics of mixtures, Appl. Sci. Res., Sect. A **3**, 279 (1952).